Neural control of steering in walking *Drosophila*

Aleksandr Rayshubskiy[1], Stephen L. Holtz[1], Isabel D'Alessandro[1], Anna A. Li[1], Quinn X. Vanderbeck[1], Isabel S. Haber[1], Peter W. Gibb[1], and Rachel I. Wilson[1,*]
[1]Department of Neurobiology, Harvard Medical School, Boston, MA, USA
*e-mail: rachel_wilson@hms.harvard.edu

Abstract: During navigation, the brain must continuously integrate external guidance cues with internal spatial maps to update steering commands. However, it has been difficult to link spatial maps with motor control. Here we identify descending "steering" neurons in the *Drosophila* brain that lie two synapses downstream from the brain's heading direction map in the central complex. These steering neurons predict behavioral turns caused by microstimulation of the spatial map. Moreover, these neurons receive "direct" sensory input that bypasses the central complex, and they predict steering evoked by multimodal stimuli. Unilateral activation of these neurons can promote turning, while bilateral silencing interferes with body and leg movements. In short, these neurons combine internal maps with external cues to predict and influence steering. They represent a key link between cognitive maps, which use an abstract coordinate frame, and motor commands, which use a body-centric coordinate frame.

Introduction

Steering is a fundamental component of navigation. Based on an animal's steering maneuvers, we can often infer what sensory cues it perceives. Steering can also be guided by working memory: many animals can steer toward a remembered spatial location. Thus, steering behavior represents a useful test case for exploring the relationship between sensory information, working memory, and motor control[1].

In vertebrates, steering maneuvers correlate with the activity of reticulospinal neurons, which are driven by locomotor control regions in the midbrain and diencephalon[2]. These brain regions are thought to have diverse context-dependent roles, reflecting context-specific inputs from higher brain centers[3,4]. It is not known whether diverse steering drives are integrated in the brain – or whether, alternatively, they are integrated in the spinal cord. Moreover, the roles of cognitive factors (like working memory) are still poorly understood, partly due to the distributed nature of the cognitive maps in the mammalian brain.

By contrast, the locus of spatial memory in the insect brain is localized to a specific region – the central complex – which drives steering toward a remembered goal. Recent studies in *Drosophila* have identified a set of "compass neurons" in this brain region which encode the fly's current heading direction[5-7]. Importantly, the mapping from heading direction onto compass neurons depends on experience, and can change within minutes[8,9]. During navigation, this compass readout is continuously compared with a remembered goal direction[10]. When compass neurons are genetically silenced, *Drosophila* can no longer steer toward an internally specified goal; remarkably, however, they can still steer directly toward a visible goal[10,11]. These results are evidence that memory-directed steering and stimulus-directed steering are mediated by distinct neural pathways.

It has been proposed that memory-directed and stimulus-directed steering drives are merged in a region of the insect brain called the lateral accessory lobe or LAL[12,13] (Fig. 1a). The LAL receives input from visual, olfactory, and auditory brain regions, in addition to input from the central complex[13]. Moreover, the LAL sends descending projections to the ventral nerve cord[13-18], the insect analog of the spinal cord. LAL descending neurons (DNs) have been studied in silkmoths and crickets, their activity correlates with steering and can influence steering[15-17]. Furthermore, in cockroaches, LAL lesions disrupt steering[19].

But are distinct steering drives actually merged in the brain? There is no evidence that individual DNs carry both memory-directed and stimulus-directed steering drives. Similarly, there is no evidence that the same DNs carry

attractive and aversive steering drives. Perhaps different DNs control steering in different contexts, and these signals are only integrated downstream, at the level of the ventral nerve cord. Indeed, some DNs seem to be recruited only in the context of a specific sensory stimulus[17,20,21].

Here we use genetically targeted whole cell recordings in walking *Drosophila* to study DNs that receive synaptic input in the LAL. We show that these neurons integrate signals for stimulus-directed steering and memory-directed steering. They lie directly postsynaptic to the central complex, as well as multiple higher-order sensory brain regions. Different DN types predict steering kinematics on distinct timescales. Finally, optogenetic manipulation of these DNs can influence body rotations and specific leg movements. In short, our results identify a site within the brain where external cues are integrated with internal drives and working memory to generate a distributed network pattern driving dynamic limb control.

Results

We chose to focus on DNs that receive synaptic input in the LAL and project to at least one leg-zone of the ventral nerve cord. A recent systematic survey[14] identified five *Drosophila* DN types that fulfill these criteria. Among these, we decided to focus on two cell types (a1 and a2; Fig. 1b), for several reasons. First, both a1 and a2 target all six leg-control zones. Given that steering involves coordinated bilateral changes in all the legs[22,23], this means that a1 and a2 are good candidates for steering DNs. Second, bilateral optogenetic stimulation of either a1 or a2 promotes walking[24]; although unilateral stimulation experiments have not been reported, this result argues that a1 and a2 have the ability to influence leg movements. Third, neurons similar to a1 and a2 are found in crickets, where they are active during walking[17,25,26].

Selective split-Gal4 lines have already been generated for a1 and a2[14]. These lines drive expression in a single cell per brain hemisphere, with occasional labeling of two cells in the a1 line. As detailed below, we found that individual a1 and a2 neurons can predict steering maneuvers in walking flies. Because a2 neurons are more predictive of steering, we will focus initially on a2; we will then proceed to compare a2 with a1.

Stimulus-directed steering

To begin, we asked whether a2 neurons are active during stimulus-directed steering maneuvers. We used the a2-selective split-Gal4 line to label these neurons with GFP, and we performed whole-cell recordings from individual a2 neurons as flies walked on a spherical treadmill (Fig. 1c). During these recordings, we presented lateralized sensory stimuli that evoke turning.

To generate attractive stimuli, we expressed the channelrhodopsin variant CsChrimson in olfactory receptor neurons under the control of an *Orco-LexA* transgene. We then stimulated the right or left antennae independently using two thin optical fibers (Fig. 1c). These fictive odor stimuli produced steering toward the stimulated antenna (Fig. 1d), consistent with previous reports using real and fictive odor[27,28]. Notably, these stimuli also produced asymmetric responses in a2, with higher firing rates on the ipsilateral side (Fig. 1d). Typically, the a2 response preceded the behavioral steering maneuver by ~100 ms (Fig. 1e). We confirmed there was no neural or behavioral response when the *LexA* transgene was omitted (Supplementary Fig. 1a).

Next, to generate aversive stimuli, we expressed CsChrimson in the antennal thermoreceptor neurons that are excited by noxious heat, under the control *Gr28b.d-LexA*. As before, we stimulated the right or left antenna independently. These fictive heat stimuli drove flies to steer away from the stimulated antenna (Fig. 1f). These stimuli again produced responses in a2, but now with higher firing rates on the contralateral side (Fig. 1f).

Thus, a2 favored the ipsilateral attractive stimulus, but the contralateral aversive stimulus. In other words, a2 encoded the laterality of the stimulus-evoked action, not the laterality of the stimulus itself. This implies a

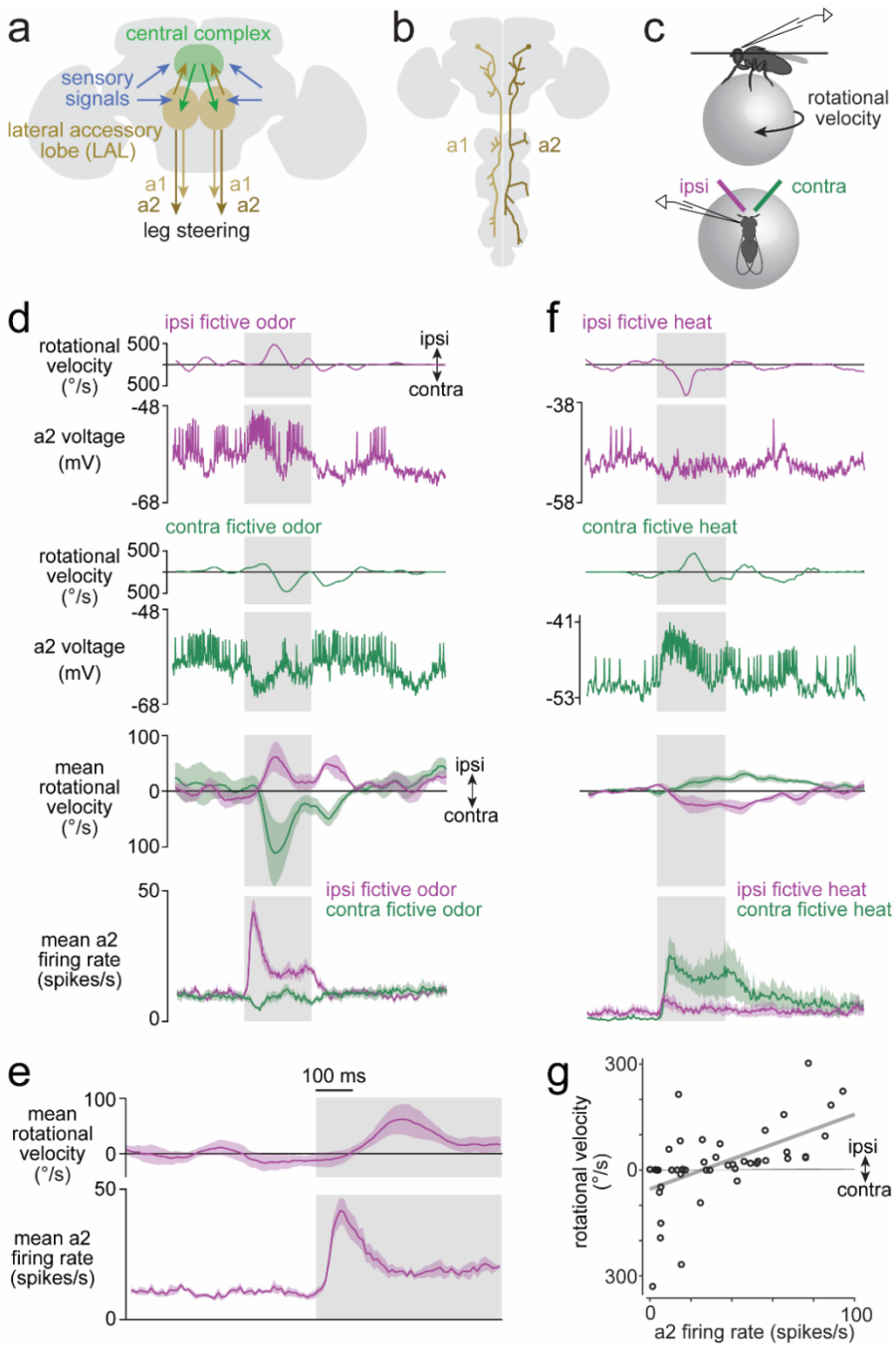

Fig. 1: Stimulus-directed steering.
a, The lateral accessory lobe (LAL) receives input from higher-order sensory brain regions, as well as the central complex, and it contains several types of descending neurons.
b, Schematic morphologies of a1 and a2. These two descending neurons have similar dendritic arbors that extend into several brain regions, including the LAL.
c, Genetically targeted recordings are performed as the fly walks on a spherical treadmill. CsChrimson is expressed in either most olfactory receptor neurons, or else all heat-sensing neurons in the antennae. A fiber-optic filament beside each antenna delivers asymmetric stimuli. Ipsi- and contralateral are defined relative to the recorded neuron.
d, Rotational velocity of the fly and a2 activity recorded simultaneously during fictive odor presentations. Top: two example trials, one ipsi and one contra. Bottom: mean ± SEM across flies, n=4 flies. Gray shading shows the 500-ms period of fictive odor.
e, Mean data on an expanded timescale to show that a2 firing rate increases precede ipsilateral turning (mean ± SEM across flies, n=4 flies).
f, Same as **d** but for fictive heat. Gray shading shows the 500-ms period of fictive heat.
g, Trial-to-trial variability in an example experiment. Each datapoint is a trial where fictive odor was presented on the ipsilateral side; gray line is linear fit (R^2=0.33, p=10^{-5}, two-tailed t-test). In other experiments, R^2 ranged from 0.16 to 0.40, with p always <0.005.

transformation from sensory coordinates to motor coordinates.

To determine whether a2 could predict trial-to-trial motor variability, we examined neural and behavioral responses to ipsilateral fictive odor. Regressing the fly's rotational velocity against a2 spike rate resulted in a strong and significant correlation across trials (Fig. 1g). This finding is additional evidence that a2 neurons primarily encode motor signals rather than sensory signals. Trial-to-trial correlations with behavior have also been reported regarding a2-like neurons in crickets[17,26].

Neural activity during immobility

Although these neurons encode motor signals, they do not fit the strong definition of "command neurons"[29]. We

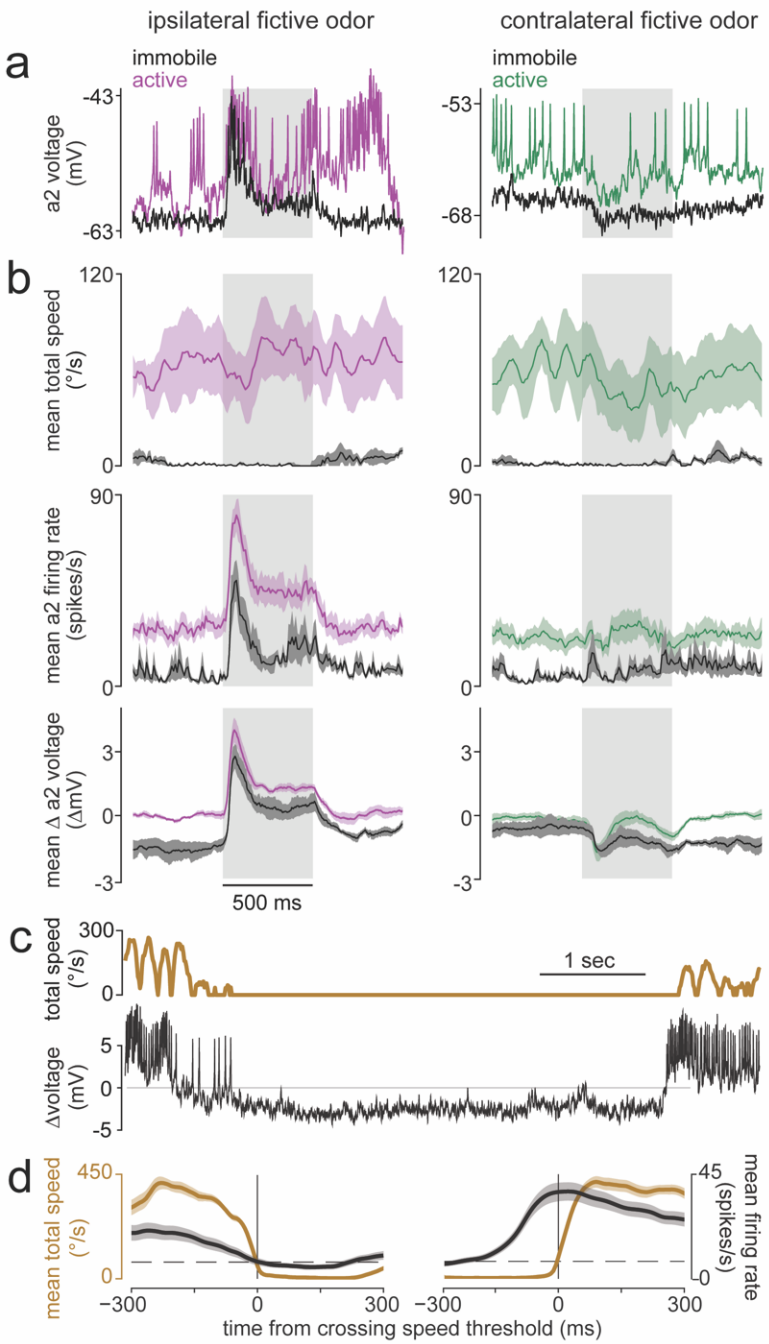

Fig. 2: Neural activity during immobility.
a, Examples of a2 activity during fictive odor presentation when the fly was active versus immobile.
b, Summary data (mean ± SEM across flies, n=4 flies) for active versus immobile trials. We defined immobility as essentially zero total speed (i.e., the sum of speed values in all three axes of ball rotation) during the 500 msec prior to stimulus onset and the entire period of stimulus presentation.
c, Example of a fly transitioning from activity to immobility, and then back to activity again.
d, Mean total speed and a2 firing rate during (left) the transition to immobility and (right) the transition to activity (± SEM across flies, n=7 flies). Transitions were detected by setting a threshold for total speed (dashed line). The firing rate change precedes the onset of movement by ~250 ms. Total speed is defined as rotational speed + sideways speed + translational speed.

would expect a steering command neuron to be unresponsive in trials where the fly was standing immobile. Contrary to this prediction, we observed stimulus-evoked responses in these neurons when the fly was immobile. Even during immobility, ipsilateral fictive odor produced depolarization, whereas contralateral fictive odor produced hyperpolarization (Fig. 2a). Moreover, the odor-evoked change in a2 firing rate was similar during walking and immobility (Fig. 2b).

To investigate this phenomenon more carefully, we identified every behavioral transition between immobility and movement. We found that the mean a2 firing rate steadily declined before a moving fly stopped (Fig. 2c,d). During this epoch, overall movement also decreased steadily, so that there was a roughly simultaneous decrease in both neural activity and movement. Conversely, behavioral transitions from immobility to movement were often relatively sharp. We found that a2 firing rates increased about 250 msec before the behavioral transition to movement, with a clear time lag between neural activity and behavior (Fig. 2c,d).

Compass steering signals

Next, we asked whether a2 neurons are recruited during compass steering driven by the central complex. The central complex produces steering signals[30] but it contains no descending neurons[14]. The LAL is thought to be the key brain region for motor control downstream from the central complex[31-34] (Fig. 1a). However, central complex output has not been linked to descending neurons.

We therefore designed an experiment to monitor a2 neurons during compass steering. To evoke steering, we microstimulated central complex neurons called P-EN1 neurons[10] by expressing the ionotropic ATP receptor $P2X_2$ in these neurons under Gal4/UAS control[35]. We briefly stimulated a few P-EN1 neurons by puffing ATP onto their dendrites (Fig. 3a). Meanwhile, to track the dynamics of the compass in real time, we expressed GCaMP6f in compass neurons (E-PG neurons) under LexA/ LexAOp control, and we imaged the entire compass neuron ensemble using volumetric two-photon microscopy.

As expected from previous work, we found that there is typically a single bump of activity in the compass neuron ensemble which rotates as the fly steers in darkness[5,6]. The position of the bump constitutes a working memory of the fly's heading direction. Again consistent with previous work[10], we found that briefly microstimulating P-EN1 neurons causes this bump to jump to a new location. This is because the normal role of P-EN1 neurons is to relay information about the fly's angular velocity to the compass neuron ensemble; thus, microstimulating P-EN1 neurons causes the compass to register a fictive behavioral turn. As a negative control, we confirmed that bump jumps rarely follow ATP injection when the Gal4 transgene is omitted (Fig. 3b).

The bump jump should create a mismatch between the fly's internal steering goal and its remembered compass heading. Accordingly, the fly typically executes a compensatory behavioral turn shortly after the bump jump[10].

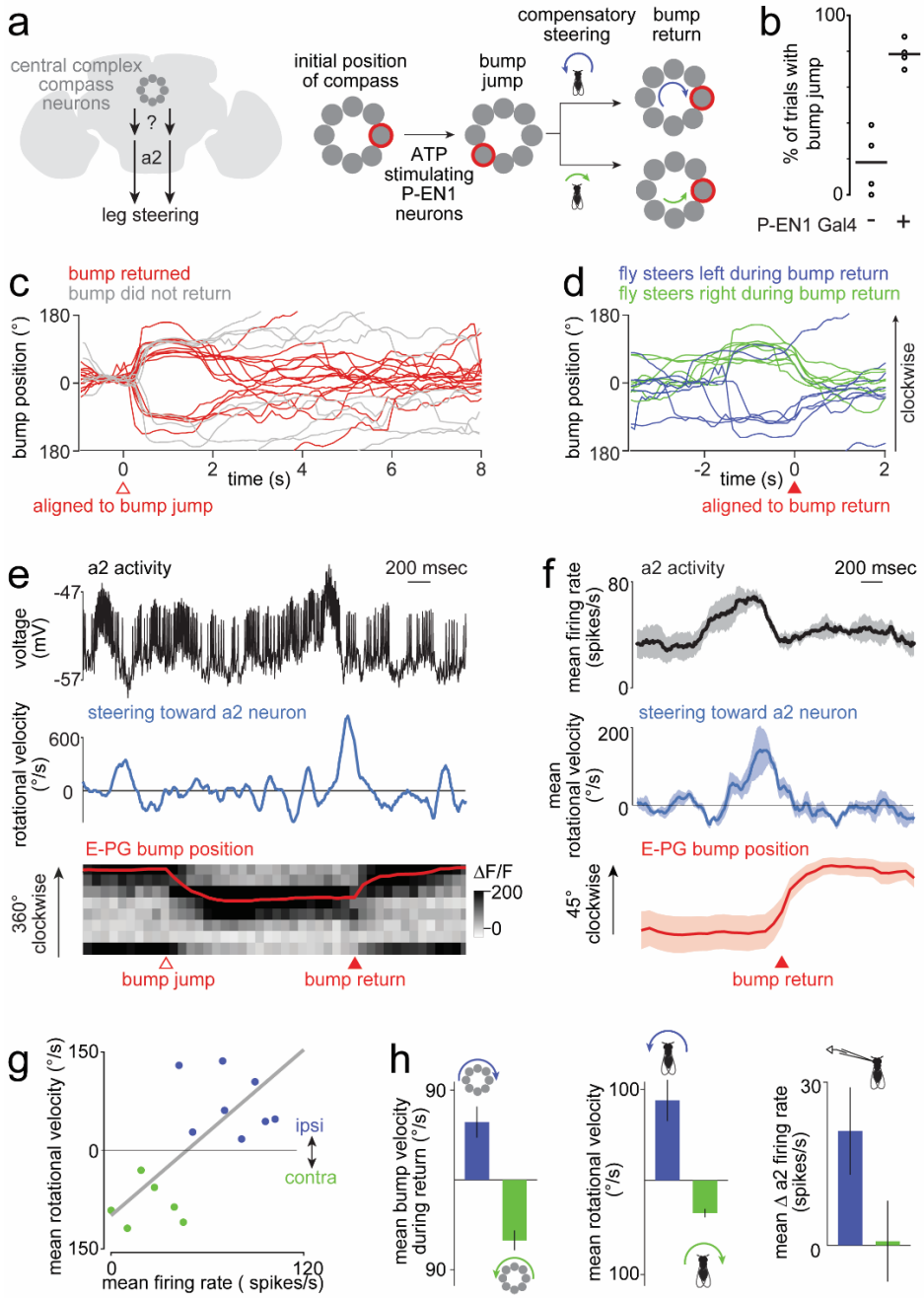

Fig. 3: Compass steering signals.

a, E-PG neurons (compass neurons) are arranged in a circle. A bump of activity (red) rotates as the fly turns. We microstimulate P-EN1 neurons with a puff of ATP (50-100 msec) to evoke a bump jump. This drives steering which returns the bump to its initial location. Meanwhile, we record from a2 in the left hemisphere.

b, Percentage of trials where a bump jump occurred after ATP. Each data point is a fly (n=4 of each genotype). In controls lacking the P-EN1 Gal4 line, the ATP puff only occasionally preceded bump jumps; this is likely coincidental, as the bump is often moving even without microstimulation.

c, Example experiment. Bump position over time is expressed relative to the mean position in the 1 sec before the ATP puff. The bump returns to its initial position in many trials (red) but not all (gray).

d, Red trials from **c** aligned to the time where the bump's return speed was maximal, color-coded according to the direction of the fly's steering just before. When the fly steered left, the bump moved clockwise, and *vice versa*.

e, Example trial. Top: a2 activity. Middle: fly's rotational velocity toward the left side, i.e., the side of the recorded a2 neuron). Bottom: E-PG activity (ΔF/F) over time; each row is a 45°-sector of the compass, with bump position in red. An ATP puff causes a bump jump (Δ). About 1s later, the left copy of a2 bursts, then the fly turns left, and then the bump returns via a clockwise path (▲).

f, Trials where the bump returned to its initial location via a clockwise path were aligned to the time of peak bump speed. Trials were averaged within a fly, and then across flies (mean ± SEM across flies, n=4 flies).

g, Trial-to-trial variability in an example experiment. Each datapoint is a trial, color-coded by the direction of the bump's return and the direction of the fly's turn. Gray line is a linear fit (R^2=0.51, p=3×10^{-3}, two-tailed t-test). In other experiments, R^2 ranged from 0.31 to 0.60, with p always <0.05.

h, Data sorted by the direction of the bump's return (mean±SEM across flies, n=4 flies). Whereas clockwise (blue) bump returns were typically preceded by leftward turning, counter-clockwise (green) bump returns were preceded by rightward turning, as expected. On average, the left copy of a2 was only excited on trials where bump moved clockwise, meaning the fly was turning left.

This turn brings the compass bump back to its initial location (Fig. 3c,d). Note that the behavioral turn can be in either direction: a leftward turn causes the bump to return clockwise, while a rightward turn causes the bump to return counter-clockwise (as viewed from the posterior side of the brain; Fig. 3a,d). On average, we found that the bump returned to its initial location in 40% of trials.

Throughout each experiment, we performed a whole-cell recording from a2. Here we used a genetically targeted fluorescent small molecule to visualize the cell for patching. This approach to labeling a2 allowed us to avoid overlap with GCaMP emission. Notably, we found that a2 cells often fired a burst of spikes just before the fly performed its compensatory behavioral turn (Fig. 3e). This result suggests that a2 participates in driving the behavioral turn, and thus lies downstream from the central complex.

To quantify this effect across trials, we identified the time point in each trial where the bump's return speed was maximal. We used this time point to align the data across trials to account for the fact that the bump's return had different latencies on different trials (Fig. 3c,d). Because we always recorded from a2 cells on the left, we focused on the trials where we expect a leftward behavioral turn – i.e., trials where the bump returned via a clockwise path. In these trials, we found that the bump jump was typically followed by increased a2 firing on the left, and then a leftward steering maneuver, and then a clockwise return of the bump (Fig. 3f).

Moreover, we found that a2 neurons could predict much of the observed variability in the magnitude of compensatory behavioral turns. Regressing the fly's rotational velocity against a2 spike rate revealed a strong and significant correlation across trials (Fig. 3g). This is additional evidence that a2 neurons are participating in driving the compensatory behavioral turn.

Trials where the bump returned in the opposite direction (counter-clockwise) provide a negative control. In these trials, the fly's behavioral turn was typically rightward rather than leftward (Fig. 3d,h). Accordingly, we found no a2 firing rate increase on the left side (Fig. 3h). This shows that a2 is not activated bilaterally and thus nonspecifically. Rather, a2 is recruited specifically on the side that predicts the direction of the behavioral turn.

In summary, a2 neurons can predict the timing of compass steering maneuvers, their direction, and their magnitude. These findings imply that a2 neurons are downstream from the central complex. This would mean that a2 is a component of the pathway that transforms working memory representations into steering maneuvers. While the major axonal projections of a2 reside in the ventral cord, a2 also sends axon collaterals to the brain[14]; it is therefore also possible that a2 neurons are part of a pathway that sends copies of motor commands back to the central complex, so that the compass can be updated after a steering maneuver.

Neurons presynaptic to descending neurons

Together, our results show that a2 neurons predict steering maneuvers in response to diverse drives – not only external sensory stimuli, but also internal "compass" drives. Are some of these drives integrated at the level of a2 neurons? Or does all this integration happen upstream from a2 neurons?

To address this question, we set out to identify a2 in an electron microscopy (EM) dataset comprising the entire *Drosophila* brain[36]. After we traced all the primary neurites in the relevant tract, we found exactly one cell that was an excellent match to a2 (Fig. 4a). We then traced the entire skeleton of a2 in the EM volume, annotating all its pre- and postsynaptic sites (Fig. 4b).

Then, we reconstructed the backbones of several hundred cells directly presynaptic to a2. We selected 28 of these cells for full reconstruction (Fig. 4c), with the goal of sampling inputs from many different brain regions. For each presynaptic cell type, we reconstructed multiple individual exemplars (Supplementary Table 1). Below we describe these cell types to illustrate their diversity.

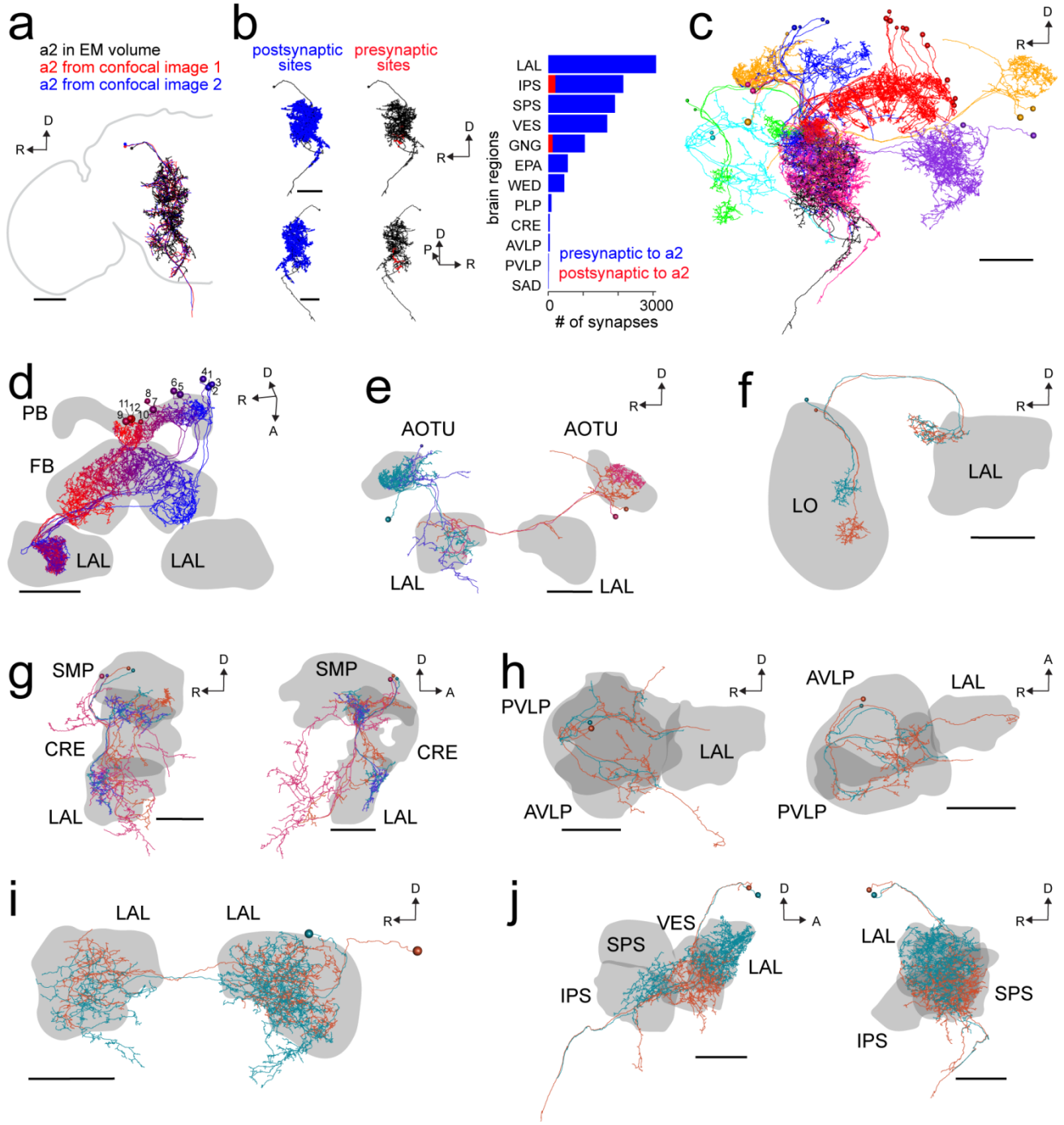

Figure 4: Convergence of internal compass cues with external sensory cues in the a2 descending neuron.
a, The cell we identified as a2 in the EM dataset (anterior view, right brain outlined), overlaid with a2 traced from confocal data. Scale bars are 50 µm (here and throughout this figure).
b, All pre- and postsynaptic sites in a2, shown from two angles (left) and tabulated by brain region (right).
c, All a2 input neurons selected for full EM reconstruction. Cell types are shown in different colors, with a2 in black.
d, Central complex output neurons (PFL3 neurons). Inputs to a2 on the right arise primarily from the left protocerebral bridge (PB). These cells have dendrite-like arbors in the PB and fan-shaped body (FB). Cells are color-coded by their position in the PB and FB.
e, Four input neurons with dendrites in the anterior optic tubercle (AOTU). Two cross the midline (magenta/orange).
f, Two input neurons with dendrites in the lobula (LO). These are lobula columnar type 9 cells (LC9).
g, Four input neurons arising from the superior medial protocerebrum (SMP) and crepine (CRE). Two project to the anterior LAL (blue/green), while the others project posteriorly. Two views are shown.
h, Two input neurons arising from the posterior/anterior ventrolateral protocerebrum (PVLP/AVLP). Two views are shown.
i, Two input neurons arising from the contralateral LAL.
j, Two DNs that provide direct input to a2. Both arborize in the LAL, vest (VES), and superior/inferior posterior slope (SPS/IPS). Two views are shown. **Supplementary Table 1** lists synapses per connection and neuron names archived at virtualflybrain.org.

Central complex. We found that a2 receives direct input from one central complex cell type (Fig. 4d). These neurons receive input in the protocerebral bridge and the fan-shaped body, and they send synaptic output to the LAL. As we were concluding this study, the FlyEM Project released a machine-annotated connectome of the dorsal-right-central portion of the female brain[37], and this dataset also includes a match to a2 (cell 1140245595). Notably, FlyEM annotations imply this same central complex cell type (called PFL3) as a major input to a2; indeed, it is second-ranked among all a2 presynaptic cell types, in terms of synapse numbers. FlyEM annotations also suggest that PFL3 neurons are positioned postsynaptic to E-PG neurons. This anatomy suggests that PFL3 neurons encode the relationship between the fly's heading and its internal goal.

Visual system. We reconstructed two cell types that project to a2 from the medial anterior optic tubercle (Fig. 4e). This structure is the largest optic glomerulus in the brain, and the only one with a retinotopic projection from the visual system[38]. Thus, these cells might participate in steering toward visual objects. We also found a cell type (LC9) that projects directly to a2 from the lobula (Fig. 4f). FlyEM annotations support the conclusion that a2 receives many direct inputs from the optic lobe and medial anterior optic tubercle.

Superior protocerebrum. We reconstructed two cell types that project to a2 from the superior medial protocerebrum and crepine (Fig. 4g). These areas are both major outputs of the mushroom body and lateral horn[39,40]. Therefore, these cells might carry olfactory and thermosensory signals to a2 neurons. Indeed, in silkmoths, cells with similar morphologies are odor-responsive[41,42]. FlyEM annotations suggest that there are many similar cell types that are presynaptic to a2.

Ventrolateral protocerebrum. We also reconstructed one cell type that projects to a2 from the anterior ventrolateral protocerebrum and the posterior ventrolateral protocerebrum (Fig. 4h). These brain regions receive auditory/mechanosensory input, as well as visual input. Both auditory and visual responses have been described in the cricket neurons[17,25,26] that resemble a2. FlyEM annotations suggest that there are many neurons like these presynaptic to a2.

Contralateral LAL. We also found that a2 receives direct input from the contralateral LAL, via LAL bilateral neurons (Fig. 4i). FlyEM annotations support this conclusion, and indeed similar cells have been described in silkmoths[13]. These cells may be involved in anticorrelating a2 activity on the left and right side of the brain.

Other DNs. We found that a2 receives direct input from other DNs (Fig. 4j). Indeed, FlyEM annotations suggest that many DNs connect to a2. DN→DN synapses may coordinate DNs with related functions.

In summary, a2 is a site where putative compass-related signals from the central complex output converge with the outputs of many brain regions that process diverse external sensory stimuli. Moreover, a2 also integrates signals from the contralateral LAL, and from other DNs. Based on our reconstructions of hundreds of primary neurites in the full-brain EM volume, we estimate that hundreds of cell types converge onto a2.

Behavioral impulse responses

Thus far, we have focused on "evoked" steering maneuvers – i.e., turns evoked by lateralized sensory stimuli, central complex stimulation, or direct optogenetic activation. However, a2 neurons are also active during spontaneous steering events. Indeed, regardless of whether steering events are spontaneous or stimulus-evoked, we found the same relationship between steering velocity and a2 spike rate (Supplementary Fig. 2).

Because we could measure many spontaneous steering events in each experiment, we used these spontaneous events to quantify the relationship between neural activity and behavioral dynamics on a fine timescale. Specifically, we computed the linear filter that describes the transformation from a2 firing rate (f) to the fly's

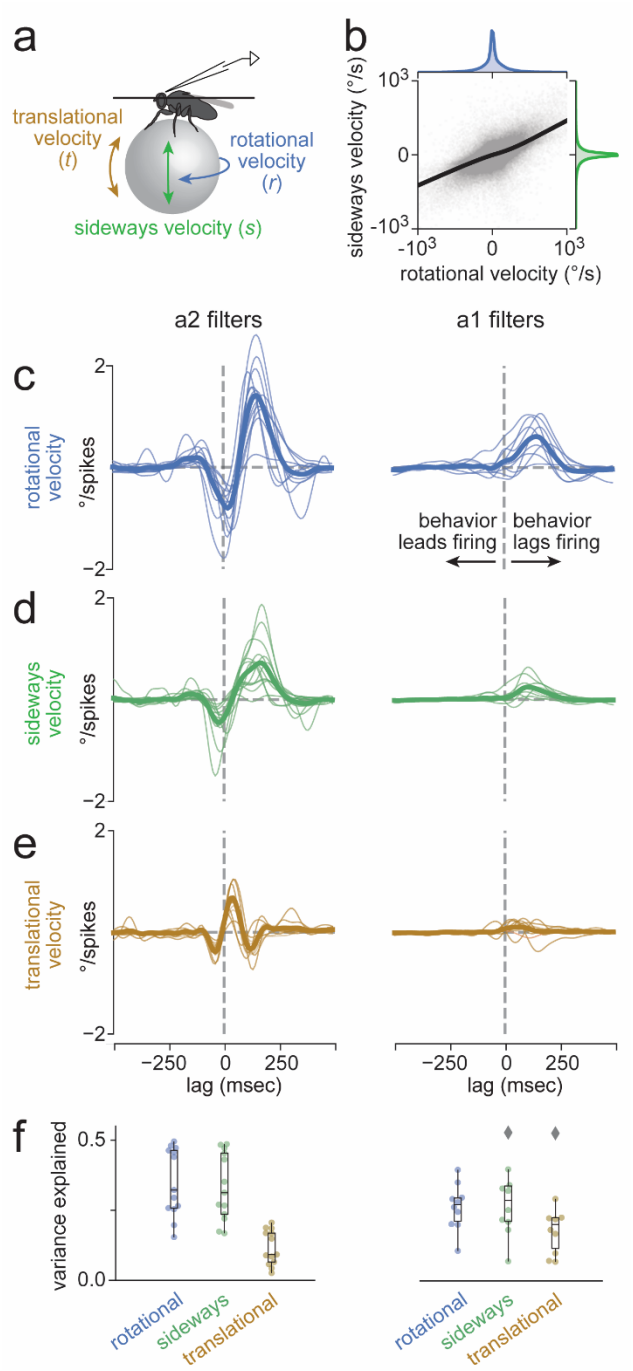

Figure 5: Behavioral impulse responses.
a, Schematic showing the three axes of movement.
b, Rotational velocity is strongly correlated with sideways velocity. Black line is a LOWESS fit; margins show kernel density estimates (20 flies).
c, Rotational velocity filters for a2 and a1. These filters describe the average rotational velocity impulse response, given a delta function (unit impulse) in firing rate. Thin lines are filters for individual flies (n=13 for a2, n=10 for a1), thick lines are averages. For positive lags, behavior follows firing; for negative lags, behavior leads firing. As expected, the filter is ~0 for negative lags. Supplementary Fig. 4 shows the reverse analysis (behavior→neuron filters).
d-e, Same for sideways and translational velocity.
f, Variance explained by each filter type. Datapoints are flies. Boxplots show interquartile range (IQR), whiskers show range of data (except for diamonds, observations >1.5×IQR).

rotational velocity (r). We cross-correlated f with r, and then normalized by the autocorrelation of f (Supplementary Fig. 4). The resulting filter tells us, on average, how rotational velocity changes after a brief increase in a2 firing rate. More precisely, it describes the rotational velocity "impulse response", given a delta function (a unit impulse) in a2 firing rate.

For comparison, we computed filters for rotational velocity (r), sideways velocity (s), and translational velocity (t; Fig. 5a). It should be noted that r and s are strongly correlated (Fig. 5b)[22,43], because many steering maneuvers involve rotation as well as side-stepping in the same direction. By contrast, neither r nor s is strongly correlated with t[22,43].

In addition to computing all these filters for a2, we did the same for a1. Notably, a1 and a2 have similar morphologies (Fig. 1b). Moreover, in pilot recordings, we found that a1 is correlated with stimulus-evoked steering events (Supplementary Fig. 3), like a2. That said, we found interesting differences in the rotational velocity (r) filters for a2 and a1 (Fig. 5c). First, the magnitude of the filter was larger for a2. This means that a unit impulse in a2 predicts a larger change in r. Second, the filter was biphasic for a2, with a negative and positive lobe having nearly equal areas. This means that a2 predicts relatively transient changes in r: if a sustained input is convolved with this sort of filter, the result is a transient output. By contrast, the r filter was monophasic for a1. This means that sustained a1 activity (unlike sustained a2 activity) predicts sustained changes in r.

Next, we considered sideways velocity (s). We found that s filters (Fig. 5d) strongly resembled r filters. This makes sense, given the correlation between s and r (Fig. 5b).

Finally, we considered translational velocity (t). We found that the t filters had relatively small amplitudes (Fig. 5e). This means that a unit impulse in a2 or a1 predicts only a small change in t. Moreover, these filters explained relatively little of the variance in behavior (Fig. 5f).

By comparison, the r and s filters explained more of the variance in behavior (Fig. 5f). In particular,

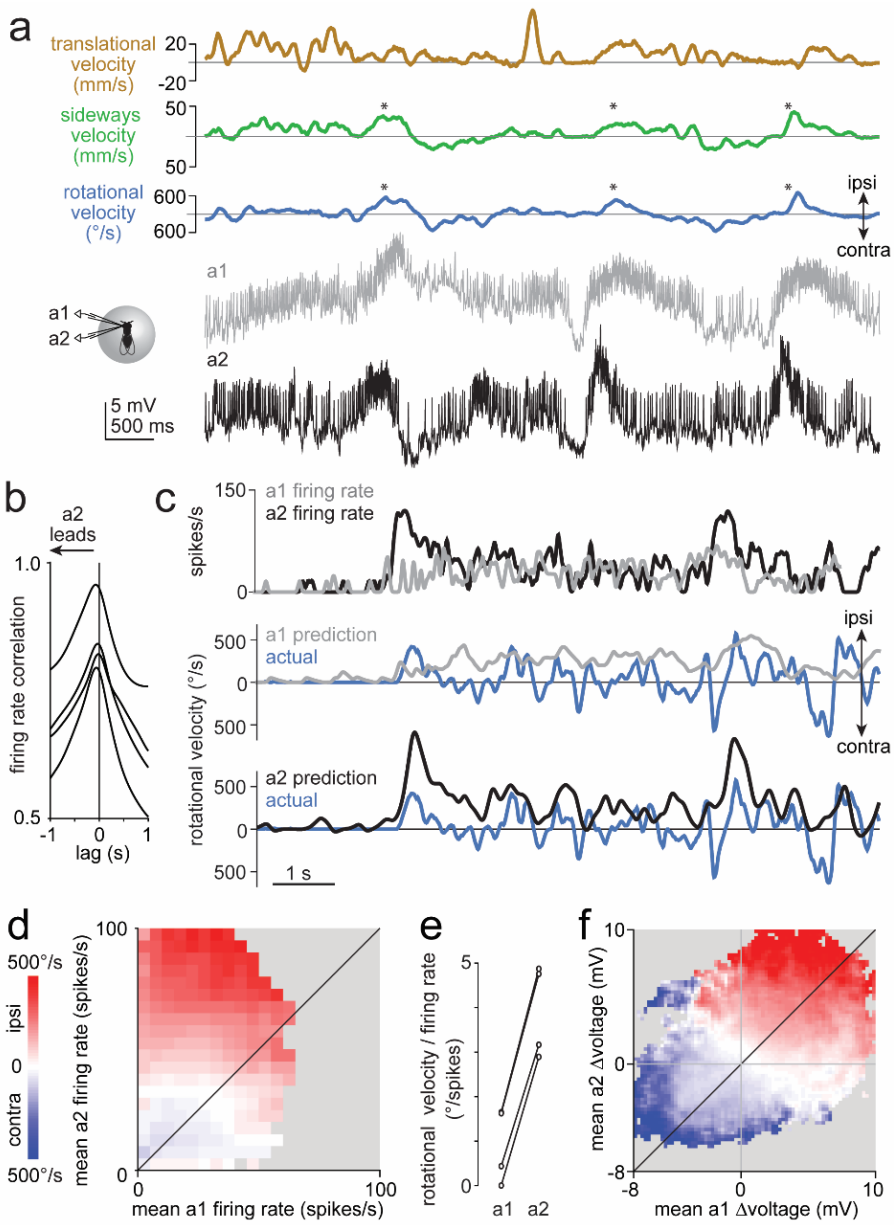

Figure 6: Dual a1/a2 recordings

a, Example dual recording from a1 and a2, both on the left. Both cells are depolarized just before the fly steers in the ipsilateral direction (asterisks). Firing rate increases tend to be more transient for a2 than for a1 (see also Supplementary Fig. 4a).

b, Correlation between a1 and a2 firing rates. Each line is a different paired recording (4 flies).

c, We computed the rotational velocity filter for each cell, and then convolved each cell's filter with its firing rate to generate rotational velocity predictions. Whereas a2 over-predicts large rapid steering events, a1 under-predicts these events.

d, Colormap shows binned and averaged rotational velocity for each value of a1 and a2 firing rates for an example paired recording. Note the plot is not symmetrical about the line of unity; instead, rotational velocity is more sensitive to a2 than to a1.

e, Slope m of the linear regression fitting rotational velocity r to each cell's firing rate f (r=mf+b). The difference between cell types is statistically significant (p=10-4, paired t-test, n=4 flies).

f, Same as (d) but for voltage changes rather than firing rate changes.

the firing rate of a typical individual a2 neuron could explain about 30% of the variance in r and s. In several recordings, the variance explained was close to 50%. This is notable, because a single a2 or a1 neuron mainly predicts ipsilateral turns, not contralateral turns. Contralateral turns are preceded by hyperpolarization and relatively small (and thus noisy) firing rate decreases; ipsilateral turns are preceded by depolarization and relatively large (and thus less noisy) firing rate increases. Thus, we would not expect single neurons to explain all the variance in turning behavior.

In summary, these analyses confirm that a2 and a1 are mainly related to steering velocity – i.e., correlated changes in rotational velocity and lateral velocity. A unit of a2 activity predicts transient, high-gain steering impulse response. By contrast, a unit of a1 activity predicts a sustained, low-gain steering impulse response.

Ensemble neural dynamics

These results motivated us to make a direct comparison between the activity patterns of a2 and a1. We first identified a Gal4 driver line that targets both a1 and a2. We then targeted both cells in the same recordings, identifying each cell based on its spike waveform, soma size, and soma position (Supplementary Fig. 5). In these experiments, we always recorded from cells on the same side of the brain, and we defined the direction of steering as ipsi- or contralateral to the recorded cells (Fig. 6a). We focused on rotational velocity as a read-out of steering behavior, because rotational and lateral velocity are highly correlated, but the signal-to-noise ratio of rotational velocity measurements is higher.

As expected, both a2 and a1 typically increased their firing rates just before the fly steered in the ipsilateral direction. However, we also noticed that a2 generally returned to baseline more rapidly

than a1 did (Fig. 6a). In other words, a2 spike bursts were more transient. This asymmetry was sufficiently large and consistent that it skewed the cross-correlation function between a2 and a1 firing rates in every paired recording (Fig. 6b).

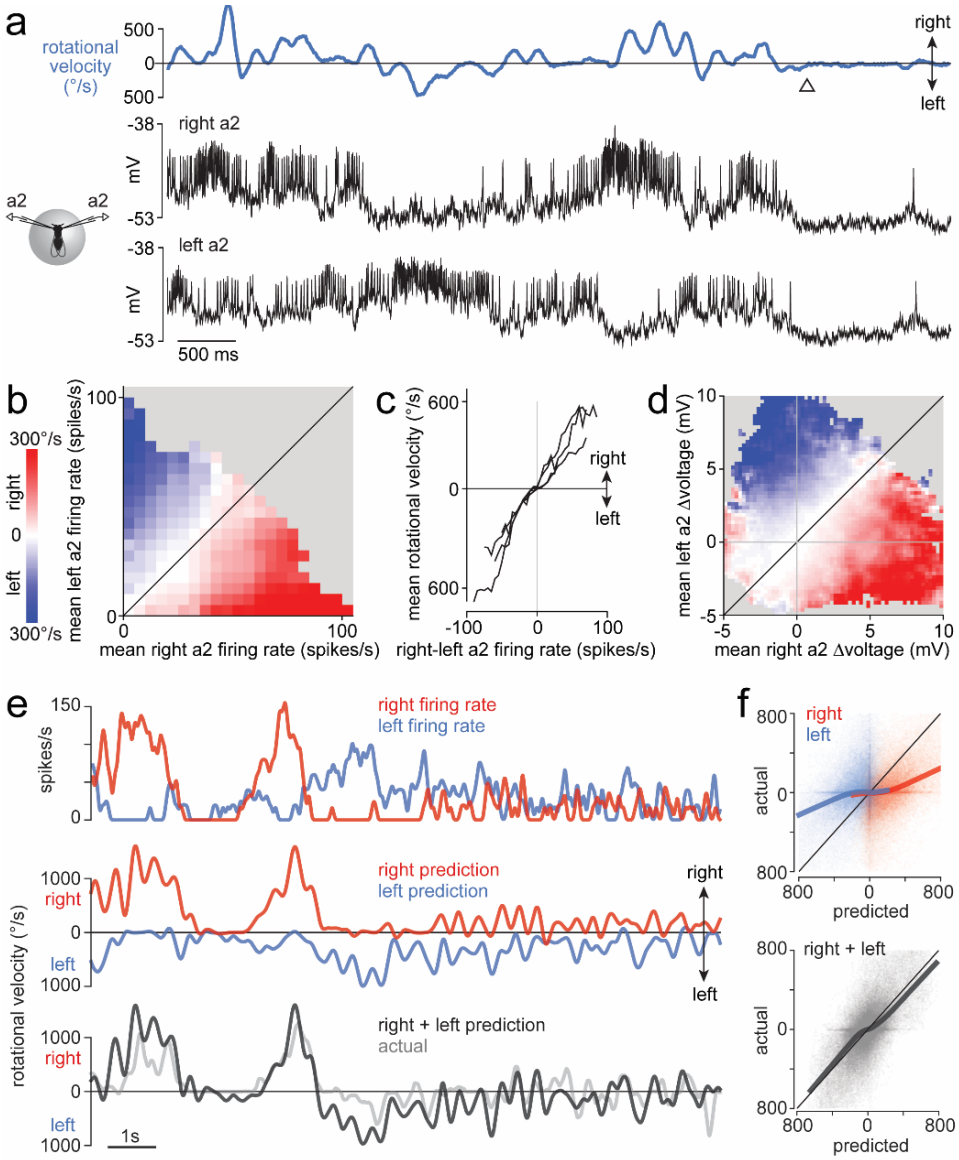

Figure 7: Dual left a2 + right a2 recordings

a, Example bilateral recording from a2. The neurons are anti-correlated when the fly is turning. Both neurons are hyperpolarized when the fly stops moving (Δ).

b, Colormap shows binned and averaged rotational velocity for each value of bilateral a2 firing rates for an example paired recording.

c, Mean rotational velocity for each value of the bilateral firing rate difference. Each line is a different paired recording (n=4 flies).

d, Same as (c) but now measuring the change in membrane voltage relative to each cell's mean. When both cells are hyperpolarized, the fly is typically immobile.

e, We computed the rotational velocity filter for each cell, and then convolved each cell's filter with its firing rate to predict rotational velocity. Combining the predictions of the two cells (with equal weighting) generates a good prediction.

f, Top: predicted rotational velocity versus actual rotational velocity, for both single-cell predictions for an example experiment. Bottom: the dual-cell prediction for this experiment. Thick lines are LOWESS fits.

We then computed rotational velocity filters for each cell, and we convolved each cell's filter with its firing rate to obtain the rotational velocity prediction for each cell. We found that a2 generally predicted large, fast fluctuations in rotational velocity. By contrast, a1 generally predicted slower, smaller fluctuations in rotational velocity (Fig. 6c).

Note that there are two factors that create this distinction. First, when we normalize for differences in neural activity dynamics, we see that a unit of a2 activity predicts a transient steering impulse response, whereas a unit of a1 activity predicts a sustained steering impulse response (Fig. 5c). Moreover, our paired recordings demonstrate that a2 activity is more transient than a1 activity (Fig. 6a). These two effects reinforce each other, and as a consequence, a2 correlates with rapid steering, while a1 correlates with slow steering.

As a complement to our analyses of neural dynamics, we also examined rotational velocity as a static function of both cell's firing rates. First, we shifted rotational velocity forward by 150 msec, to account for the average time lag between neural activity and behavior (Fig. 5c). We then divided each experiment into 50-msec windows, and we computed mean firing rates and rotational velocity within each window. Finally, we binned and averaged rotational velocity according to the firing rates of both cells. This produced a map of rotational velocity in a2/a1 coordinates (Fig. 6d). This map

showed that rotational velocity is a relatively steep function of the a2 firing rate, but a shallower function of a1 firing rate (Fig. 6d,e), directly confirming our predictions based on relative filter amplitudes (Fig. 5c). This result further supports the notion that a2 spikes exert more influence over steering velocity than a1 spikes do.

Interestingly, both a2 and a1 were hyperpolarized during contralateral turns (Fig. 6f). Here again, the gain of the behavior-neuron relationship was steeper for a2 than for a1. This suggests that steering is particularly correlated with right-left asymmetries in a2 activity.

To test this prediction, we made paired recordings from a2 neurons on the left and right (Fig. 7a). We used these recordings to compute a map of rotational velocity in right-left coordinates, using the procedure described above. We found that rotational velocity was consistently related to the difference in right-left firing rates (Fig. 7b). This relationship was essentially linear through its entire dynamic range, and was quite consistent across paired recordings (Fig. 7c). The difference in right-left membrane voltage was also linearly related to rotational velocity (Fig. 7d).

Although right-left a2 pairs were anti-correlated during steering, they could be positively correlated in some situations. In particular, right-left pairs hyperpolarized together just before the fly stopped moving, and they depolarized together just before the fly began moving again (Fig. 7a and Supplementary Fig. 6). Interestingly, when a1 was more hyperpolarized than a2, the fly was generally moving backward (Supplementary Fig. 7).

Finally, we used a linear filter analysis to probe the relationship between neural activity and behavioral dynamics in right-left pairs (Fig. 7e). We used each neuron's firing rate and linear filter to compute the fly's predicted rotational velocity. As we might expect, this showed that each cell was mainly predictive of steering in the direction ipsilateral to that cell, with weak predictive power in the contralateral direction. We could accurately predict turns in both directions by linearly combining the two predictions (Fig. 7f).

In short, our results show that different neurons predict distinct features of steering behavior. Different cell types (a2 versus a1) predict steering on different time scales. Meanwhile, the difference in activity between the right-left copies of the same cell type predicts steering in the right and left directions.

Unilateral activation of descending neurons

Next, to determine if these neurons can actually influence steering, we used hs-FLP to stochastically express a channelrhodopsin variant (ReaChR) in a2 neurons. This produced either unilateral expression (16 flies) or bilateral expression (17 flies; Fig. 8a). As each fly walked on a spherical treadmill, we illuminated its head from above to activate the ReaChR+ neuron(s). This illumination was symmetric on the two sides of the head.

In the 16 flies with unilateral expression, we found that light evoked a small average turning bias in the ipsilateral direction – i.e., the direction of the activated neuron (Fig. 8b). To determine if this bias was significant, we used sibling flies with bilateral expression as controls. Specifically, each fly with bilateral expression was randomly assigned a label ("right expression" or "left expression"). Using these flies, we then computed the average rotational velocity in the "ipsilateral" direction, just as we did for the flies with true unilateral expression. This simulation was repeated independently for 1000 bootstrap replicates (resampling with replacement) to obtain the 95% confidence interval of the mean, under the null hypothesis that there is only a random relationship between a2 expression and steering behavior. We found that the mean of the data (with unilateral expression) was outside the 95% confidence interval of the simulation outcomes (Fig. 8b,c). Thus, in flies with unilateral expression, the turning bias is significantly larger than the bias in control flies with bilateral expression.

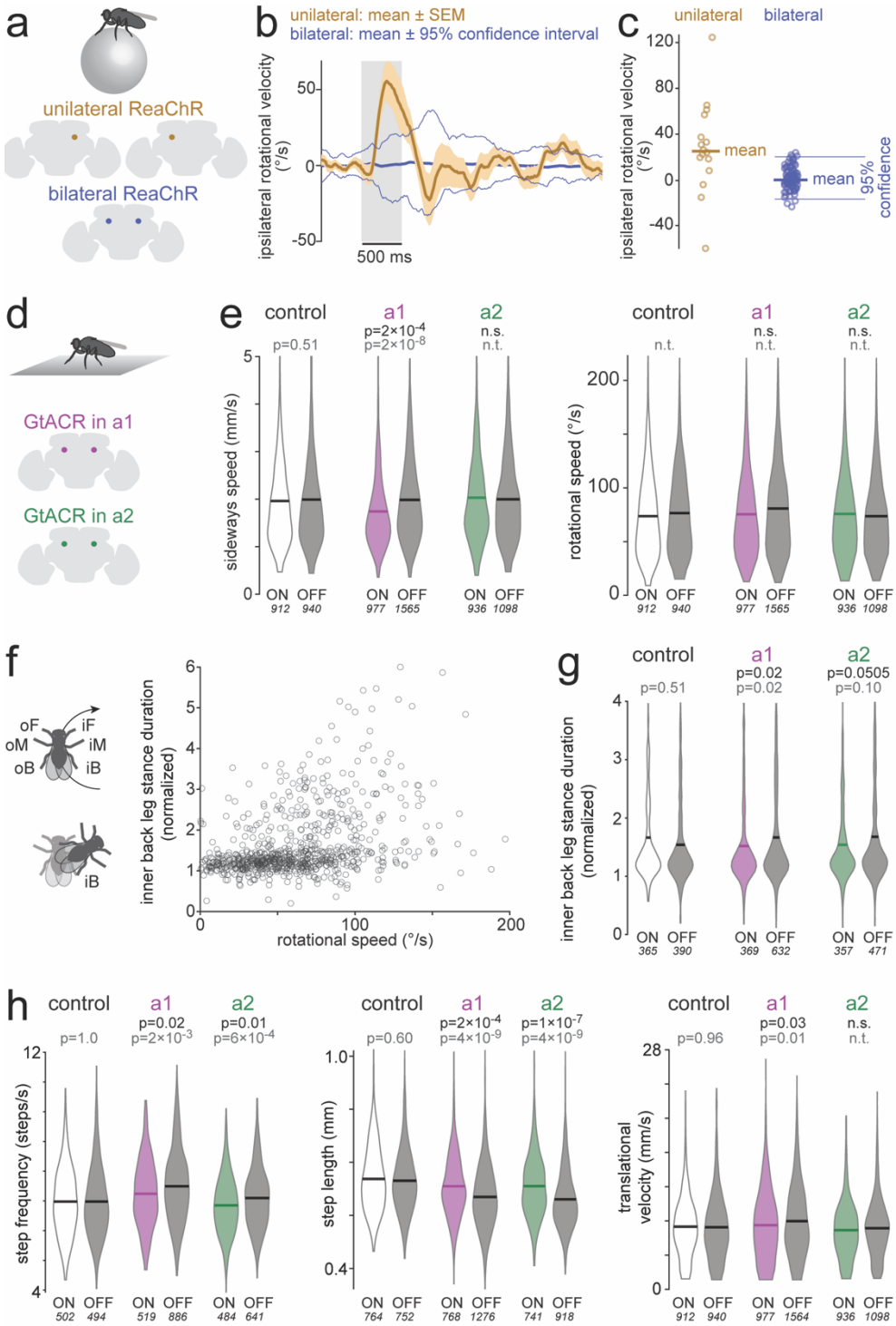

Fig. 8: DN optogenetic manipulations.
a, As flies walked on a spherical treadmill, they were illuminated repeatedly for 500-ms epochs. ReaChR was expressed uni- or bilaterally in a2.
b, Ipsilateral rotational velocity, mean of 16/17 flies (unilateral/bilateral ReaChR). The mean of the unilateral data (thick gold line) lies outside the 95% confidence interval (thin blue lines) of the distribution of outcomes we obtain when we randomly assign bilateral (control) flies to the "right" or "left" expression group.
c, Ipsilateral rotational velocity. Each data point is one fly (or simulated fly), averaged across the illumination epoch.
d, GtACR1 was expressed bilaterally in a1 or a2. Flies were illuminated repeatedly for 2-min epochs as they walked in an arena.
e, Sideways and rotational speed distributions for light on/off in each genotype. The p-values in black denote ANOVA genotype×light interactions after Bonferroni-Holm correction; the p-values in gray denote post hoc Tukey tests comparing light on/off within a genotype; n.s. = not significant, n.t. = not tested (because genotype×light interaction was not significant). The number of points (500-ms time windows) in each distribution is shown in italics; see Methods for fly numbers.
f, Stance duration of inner back (iB) leg, normalized to other legs (oF, oM, oB, iF) was measured in 500-ms time windows (n=755 windows) and plotted versus rotational speed. For some windows where rotational speed is high, iB stance duration is prolonged i.e., the fly pivots on its iB leg.
g, Distribution of normalized iB stance durations, for 500-ms time windows where rotational speed exceeded a threshold of 20 °/s for ≥100 ms.
h, Step frequency, step length, and translational velocity distributions.

In these experiments, symmetric illumination from above also caused changes in forward velocity. These effects were likely due to visual startle, because they were indistinguishable in flies with unilateral expression, bilateral expression, and no expression (data not shown). Due to the confounding effect of visual startle, we could not use this dataset to investigate how optogenetic activation of a2 affects the fly's forward velocity.

Bilateral silencing of descending neurons

To investigate the effect of bilateral DN silencing, we expressed an inhibitory opsin (GtACR1) in either a1 neurons or a2 neurons (Fig. 8d). As a genetic control, we also used an "empty" split-Gal4 line. As each fly walked in a small arena, we switched an overhead light on and off periodically (2 min on, 2 min off). We analyzed

behavior as a function of genotype (Gal4/control) and light (on/off) using a set of two-factor ANOVAs, corrected for multiple comparisons. A significant (genotype×light) interaction would be evidence for a behavioral effect of DN silencing.

First, we analyzed the body movements that are correlated with a1 and a2 activity – namely, rotational and sideways movements (Fig. 8e). When a1 neurons were silenced, sideways speed was significantly reduced. Surprisingly, however, rotational speed was unchanged when either a1 or a2 neurons were silenced.

Recall that a1 and a2 predict rotational movements about as well as they predict sideways movements (Fig. 5f). Moreover, unilateral activation of a2 influences ipsilateral rotational speed (Fig. 8b,c). Why, then, is rotational speed unaltered when these DNs are bilaterally silenced? Importantly, body rotation can be achieved via many different leg maneuvers[22,23]. For example, in some body-rotation events, the stance duration of the inner back leg is prolonged relative to the other legs – in essence, the fly pivots on its inner back leg – whereas this maneuver is absent in other body-rotation events (Fig. 8f). Perhaps DN silencing interferes with a specific leg maneuver, rather than body rotation *per se*.

To investigate this idea, we identified five leg maneuvers that often accompany body rotations in control flies (Supplementary Fig. 8). We then examined whether each leg maneuver was altered by DN silencing. Interestingly, we found that silencing a1 produced a significant defect in stance prolongation in the inner back leg – i.e., it reduced the fly's tendency to pivot on the inner back leg (Fig. 8g). We observed the same result when we silenced a2, although here the result fell just short of our cutoff for statistical significance. These results imply that silencing a1 (or possibly a2) causes a defect in inner-back-leg-stance-prolongation, but this defect is compensated via other mechanisms to achieve the same target rotational speed.

Finally, we noticed that silencing either a1 or a2 decreased the fly's bilateral step frequency, while also increasing bilateral swing distance (Fig. 8h). Silencing a1 also decreased the fly's translational velocity. Notably, all these results phenocopy the consequences of proprioceptor ablation[44]. These results are consistent with the idea that DNs modulate walking by controlling the gain of proprioceptive reflex loops[42,43]. Specifically, we propose that lateralized DN activity produces lateral asymmetries in proprioceptive reflexes, leading to asymmetric leg movements, and thus turning.

Discussion

Ensemble codes for motor control

At the outset of this study, we hypothesized that a1 and a2 would play similar roles in steering. It was already known that both cell types receive synaptic input in the LAL[14], and also project to all three sets of leg-control neuropils in the ventral cord[14]. Indeed, we found that a1 and a2 both correlate with rotational velocity and sideways velocity in the ipsilateral direction (Fig. 5). Moreover, bilateral silencing of either a1 or a2 decreases the tendency of flies to rotate by pivoting on their inner back leg (Fig. 8g).

We also found evidence that a1 and a2 have non-identical functions. Specifically, we found that a2 predicts large, rapid steering events, whereas a1 predicts smaller and slower steering events (Figs. 5 and 6). In addition, we found that silencing a1 decreases sideways speed (Fig. 8e), whereas silencing a2 does not. Notably, a1 and a2 have distinct axonal projection patterns[14] (Fig. 1b), suggesting they have non-identical downstream targets. Whereas a1 terminates in the medial part of the leg neuropil, a2 projects through the entire medial-lateral extent[14] (Figure 1b). Given the myotopic map of motorneuron dendrites within each leg neuropil[45], a1 may influence motorneurons controlling proximal leg muscles, whereas a2 may influence motorneurons controlling the entire leg.

It seems likely that a1 and a2 are not the only DNs with roles in steering. Based on the recent systematic survey of Namiki et al.[14], there are 22 known DN types that (like a1 and a2) individually target all the leg-control regions of the cord. Most of these cell types exist as one cell per brain hemisphere. Because Namiki et al. surveyed about half of all DN types, the true number of relevant cell types is probably larger. In the future, it will be interesting to develop a more complete picture of the neural code for steering at the level of DN populations. Ultimately, we want to know how these neurons work together to control leg movements – and wing movements during in-flight steering[46]. This understanding will allow us to re-frame the problem of motor control as a problem of generating specific dynamical patterns of ensemble neural activity.

In this regard, it is notable that the a2 still exhibits weak stimulus-evoked responses during rest, even when flies appear motionless (Fig. 2). Similarly, a recent study found that DNs that evoke landing during flight are still responsive to visual stimuli when the fly is not flying[47]. We might think of these weak DN responses as a latent bias toward action, or a partial preparation for an action that never ultimately occurs[48]. In this regard, it is relevant that mammalian corticospinal neurons can be active in the absence of movement, either in the period preceding a movement[49] or when a movement is being simply observed[50]. These latent corticospinal signals may represent movement preparation, which may additionally involve neurons which are not active during movement *per se*[51].

Transformations across coordinate frames

Our results demonstrate that a2 predicts not only stimulus-directed steering (Figs. 1 and 2) but also memory-directed steering. Specifically, we show that a2 predicts compensatory steering maneuvers evoked by artificial rotation of the representation of heading direction in working memory (Fig. 3). Indeed, using EM reconstructions, we demonstrate that a2 is a node of anatomical convergence between higher-order sensory neurons and central complex output neurons (Fig. 4).

The implication of our results is that a2 integrates information from sensory coordinate frames and "cognitive" coordinate frames. Cognitive goals, such as remembered objects or arbitrary angles from landmarks, are likely referenced to the brain's internal representation of heading direction. In the *Drosophila* brain, this representation is abstract and flexible: a particular E-PG neuron may represent different heading angles in different individuals[5], and experience-dependent plasticity can change this mapping[8,9]. A similarly flexible coordinate frame is also found in mammalian head direction cells: when the animal is moved to a new environment, head direction cells switch their preferred directions[52]. How a flexible, abstract representation of heading angle can drive steering is not well-understood.

Here we show that DNs in the LAL are involved in the control of steering by the central complex, and we demonstrate that these DNs employ a consistent action-centric reference frame. This contrasts with the flexible coordinate frame of compass neurons (E-PG neurons). On the basis of our results, we propose that the transformation from flexible, cognitive coordinates to consistent, action-centric coordinates occurs at the interface between E-PG neurons and steering DNs. Moreover, we identify a novel cell type (PFL3) which forms a remarkably direct connection from E-PG neurons to steering DNs. In the future, it will be interesting to investigate the roles of these neurons in the transformation from cognition to action.

Author Contributions: A.R. and R.I.W. designed the study. A.R. built all experimental devices and performed all experiments. S.L.H. performed the analyses in Figs. 2d, 5, 6c, and 7e,f, as well as Supplementary Figs. 4 and 7c. I.D. performed analyses and visualizations of EM reconstructions in Fig. 4. A.A.L., Q.X.V., I.S.H., and P.W.G. reconstructed neurons from EM data in Fig. 4. A.R. performed all other analyses. A.R. and R.I.W. wrote the manuscript with input from S.L.H. and I.D.

Acknowledgments: We are grateful to Gwyneth Card, Michael Dickinson, Hiro Namiki, and Wyatt Korff for sharing descending neuron morphology data and split-Gal4 drivers (*SS00730* and *SS00731*) pre-publication. Luke D. Lavis and Jonathan B. Grimm provided SiR110-HaloTag dye pre-publication. Julian Ng, Sebastian Cachero, and Gregory Jefferis shared *pJFRC81-td3-Halo7::CAAX(attP18)* flies pre-publication. Tzumin Lee shared *Orco-LexA* flies, Marco Gallio shared *Gr28b.d-LexA* flies, Gero Miesenböck shared *UAS-P2X*$_2$ flies, Tom Clandinin shared *hsFLP.70* flies, and Mike Crickmore shared *UAS-GtACR1::eYFP(VK00005)* flies. Jonathan Green provided excellent advice on central complex stimulation. Tom Kazimiers helped transfer our EM reconstructions to the FAFB-v14 community workspace. Mert Erginkaya, Saba Ali, Kelli Fairbanks, Tansy Yang, Emily Tenshaw, Markus Pleijzier, Imaan Tamimi, Eugenia Chiappe, Vivek Jayaraman, Barry Dickson, Gwyneth Card, and Greg Jefferis contributed to reconstructing neurons in Fig. 4. Douglas Hayden provided statistical advice. Members of the Wilson lab provided feedback on the manuscript. A.R. is supported by National Research Service Award 5F31DC015701. S.L.H. is supported by a National Research Service Award 5F31NS106982. This work is supported by NIH grants R01DC008174, R01NS101157, and U19NS104655. R.I.W. is an HHMI Investigator.

References

1. Schöne, H. *Spatial Orientation: The Spatial Control of Behavior in Animals and Man* (Princeton University Press, Princeton, NJ, 2014).
2. Ferreira-Pinto, M.J., Ruder, L., Capelli, P. & Arber, S. Connecting circuits for supraspinal control of locomotion. *Neuron* **100**, 361-374 (2018).
3. Jordan, L.M. Initiation of locomotion in mammals. *Ann. N. Y. Acad. Sci.* **860**, 83-93 (1998).
4. Caggiano, V.*, et al.* Midbrain circuits that set locomotor speed and gait selection. *Nature* **553**, 455-460 (2018).
5. Seelig, J.D. & Jayaraman, V. Neural dynamics for landmark orientation and angular path integration. *Nature* **521**, 186-191 (2015).
6. Green, J.*, et al.* A neural circuit architecture for angular integration in *Drosophila*. *Nature* **546**, 101-106 (2017).
7. Kim, S.S., Rouault, H., Druckmann, S. & Jayaraman, V. Ring attractor dynamics in the Drosophila central brain. *Science* **356**, 849-853 (2017).
8. Fisher, Y.E., Lu, J., D'Alessandro, I. & Wilson, R.I. Sensorimotor experience remaps visual input to a heading direction network. *Nature* **576**, 121-125 (2019).
9. Kim, S.S., Hermundstad, A.M., Romani, S., Abbott, L.F. & Jayaraman, V. Generation of stable heading representations in diverse visual scenes. *Nature* **576**, 126-131 (2019).
10. Green, J., Vijayan, V., Mussells Pires, P., Adachi, A. & Maimon, G. A neural heading estimate is compared with an internal goal to guide oriented navigation. *Nat. Neurosci.* **22**, 1460-1468 (2019).
11. Giraldo, Y.M.*, et al.* Sun navigation requires compass neurons in *Drosophila*. *Curr. Biol.* **28**, 2845-2852 e2844 (2018).
12. Wolff, G. & Strausfeld, N.J. The insect brain: a commentated primer. in *Structure and Function of Invertebrate Nervous Systems* (ed. A. Schmidt-Rhaesa, S. Harzsch & G. Purschke) 597–639 (Oxford University Press, Oxford, 2016).
13. Namiki, S. & Kanzaki, R. Comparative neuroanatomy of the lateral accessory lobe in the insect brain. *Front. Physiol.* **7** (2016).
14. Namiki, S., Dickinson, M.H., Wong, A.M., Korff, W. & Card, G.M. The functional organization of descending sensory-motor pathways in *Drosophila*. *eLife* **7**, e34272 (2018).
15. Olberg, R.M. Pheromone-triggered flip-flopping interneurons in the ventral nerve cord of the silkworm moth, Bombyx mori. *J. Comp. Physiol.* **152**, 297-307 (1983).
16. Zorović, M. & Hedwig, B. Descending brain neurons in the cricket *Gryllus bimaculatus* (de Geer): auditory responses and impact on walking. *J. Comp. Physiol. [A].* **199**, 25-34 (2013).
17. Staudacher, E. & Schildberger, K. Gating of sensory responses of descending brain neurones during walking in crickets. *J. Exp. Biol.* **201**, 559 (1998).
18. Bidaye, S.S., Machacek, C., Wu, Y. & Dickson, B.J. Neuronal control of *Drosophila* walking direction. *Science* **344**, 97 (2014).
19. Harley, C.M. & Ritzmann, R.E. Electrolytic lesions within central complex neuropils of the cockroach brain affect negotiation of barriers. *J. Exp. Biol.* **213**, 2851 (2010).
20. Böhm, H. & Schildberger, K. Brain neurones involved in the control of walking in the cricket *Gryllus bimaculatus*. *J. Exp. Biol.* **166**, 113-130 (1992).
21. Burdohan, J.A. & Comer, C.M. Cellular organization of an antennal mechanosensory pathway in the cockroach, *Periplaneta americana*. *J. Neurosci.* **16**, 5830-5843 (1996).
22. DeAngelis, B.D., Zavatone-Veth, J.A. & Clark, D.A. The manifold structure of limb coordination in walking *Drosophila*. *eLife* **8** (2019).
23. Strauss, R. & Heisenberg, M. Coordination of legs during straight walking and turning in Drosophila melanogaster. *J Comp Physiol A* **167**, 403-412 (1990).
24. Cande, J.*, et al.* Optogenetic dissection of descending behavioral control in *Drosophila*. *eLife* **7**, e34275 (2018).

25. Brodfuehrer, P.D. & Hoy, R.R. Ultrasound sensitive neurons in the cricket brain. *J. Comp. Physiol. [A].* **166**, 651-662 (1990).
26. Zorović, M. & Hedwig, B. Processing of species-specific auditory patterns in the cricket brain by ascending, local, and descending neurons during standing and walking. *J. Neurophysiol.* **105**, 2181-2194 (2011).
27. Borst, A. & Heisenberg, M. Osmotropotaxis in *Drosophila melanogaster*. *J. Comp. Physiol. [A].* **147**, 479-484 (1982).
28. Gaudry, Q., Hong, E.J., Kain, J., de Bivort, B. & Wilson, R.I. Asymmetric neurotransmitter release at primary afferent synapses enables rapid odor lateralization in *Drosophila*. *Nature* **493**, 424-428 (2013).
29. Kupfermann, I. & Weiss, K.R. The command neuron concept. *Behav. Brain Sci.* **1**, 3–39 (1978).
30. Martin, J.P., Guo, P., Mu, L., Harley, C.M. & Ritzmann, R.E. Central-complex control of movement in the freely walking cockroach. *Curr. Biol.* **25**, 2795-2803 (2015).
31. Hanesch, U., Fischbach, K.F. & Heisenberg, M. Neuronal architecture of the central complex in *Drosophila melanogaster*. *Cell Tissue Res.* **257**, 343–366 (1989).
32. Shih, C.T.*, et al.* Connectomics-based analysis of information flow in the *Drosophila* brain. *Curr. Biol.* **25**, 1249-1258 (2015).
33. Wolff, T., Iyer, N.A. & Rubin, G.M. Neuroarchitecture and neuroanatomy of the *Drosophila* central complex: A GAL4-based dissection of protocerebral bridge neurons and circuits. *J. Comp. Neurol.* **523**, 997-1037 (2015).
34. Lin, C.-Y.*, et al.* A comprehensive wiring diagram of the protocerebral bridge for visual information processing in the *Drosophila* brain. *Cell Rep.* **3**, 1739-1753 (2013).
35. Lima, S.Q. & Miesenböck, G. Remote control of behavior through genetically targeted photostimulation of neurons. *Cell* **121**, 141-152 (2005).
36. Zheng, Z.*, et al.* A complete electron microscopy volume of the brain of adult *Drosophila* melanogaster. *Cell* **174**, 730-743 (2018).
37. Xu, C.S.*, et al.* A connectome of the adult Drosophila central brain. *bioRxiv* **2020.01.21.911859** (2020).
38. Wu, M.*, et al.* Visual projection neurons in the Drosophila lobula link feature detection to distinct behavioral programs. *eLife* **5** (2016).
39. Aso, Y.*, et al.* The neuronal architecture of the mushroom body provides a logic for associative learning. *eLife* **3**, e04577 (2014).
40. Frechter, S.*, et al.* Functional and anatomical specificity in a higher olfactory centre. *eLife* **8**, e44590 (2019).
41. Kanzaki, R., Arbas, E.A. & Hildebrand, J.G. Physiology and morphology of protocerebral olfactory neurons in the male moth *Manduca sexta*. *J. Comp. Physiol. [A].* **168**, 281-298 (1991).
42. Namiki, S., Iwabuchi, S., Pansopha Kono, P. & Kanzaki, R. Information flow through neural circuits for pheromone orientation. *Nature Commun.* **5**, 5919 (2014).
43. Katsov, A.Y., Freifeld, L., Horowitz, M., Kuehn, S. & Clandinin, T.R. Dynamic structure of locomotor behavior in walking fruit flies. *eLife* **6** (2017).
44. Mendes, C.S., Bartos, I., Akay, T., Marka, S. & Mann, R.S. Quantification of gait parameters in freely walking wild type and sensory deprived Drosophila melanogaster. *eLife* **2**, e00231 (2013).
45. Brierley, D.J., Rathore, K., VijayRaghavan, K. & Williams, D.W. Developmental origins and architecture of Drosophila leg motoneurons. *J. Comp. Neurol.* **520**, 1629-1649 (2012).
46. Schnell, B., Ros, I.G. & Dickinson, M.H. A descending neuron correlated with the rapid steering maneuvers of flying Drosophila. *Curr. Biol.* **27**, 1200-1205 (2017).
47. Ache, J.M., Namiki, S., Lee, A., Branson, K. & Card, G.M. State-dependent decoupling of sensory and motor circuits underlies behavioral flexibility in *Drosophila*. *Nat. Neurosci.* **22**, 1132-1139 (2019).
48. Kien, J. Neuronal activity during spontaneous walking—I. Starting and stopping. *Comp. Biochem. Physiol., Part A Mol. Integr. Physiol.* **95**, 607-621 (1990).
49. Tanji, J. & Evarts, E.V. Anticipatory activity of motor cortex neurons in relation to direction of an intended movement. *J. Neurophysiol.* **39**, 1062-1068 (1976).
50. Kraskov, A.*, et al.* Corticospinal mirror neurons. *Philos. Trans. R Soc. Lond. B Biol. Sci.* **369**, 20130174 (2014).

51. Churchland, M.M., Cunningham, J.P., Kaufman, M.T., Ryu, S.I. & Shenoy, K.V. Cortical preparatory activity: Representation of movement or first cog in a dynamical machine? *Neuron* **68**, 387-400 (2010).
52. Mizumori, S.J. & Williams, J.D. Directionally selective mnemonic properties of neurons in the lateral dorsal nucleus of the thalamus of rats. *J. Neurosci.* **13**, 4015-4028 (1993).

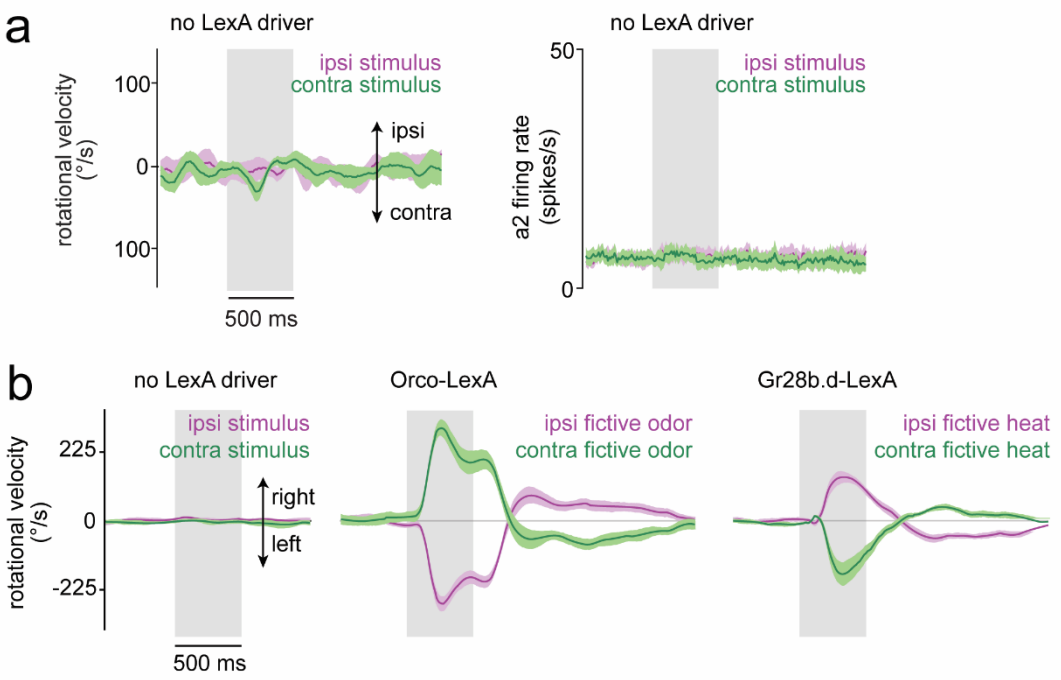

Supplementary Figure 1: Genetic controls for fictive sensory stimuli and behavioral responses in intact flies

a, Rotational velocity (left) and a2 firing rate (right) in genetic control flies where no LexA transgene was present (mean ± SEM across flies, n=4 flies). These flies were treated just like those in Fig. 1, meaning that each antenna was illuminated in the same way. There is essentially no steering behavior or a2 response. This result confirms that the steering behavior and a2 responses we describe in Fig. 1 are not due to the visual or thermal effects of the fiber optic illumination *per se*. The lack of visual responses is likely related to the fact that the fiber optic filament is very small (50 µm diameter), and the illumination from the fiber is partially blocked by the antenna, which is positioned very close to the fiber.

b, Behavioral responses in flies where no dissection was performed, i.e. we did not open the head capsule. Left: genetic controls lacking a *LexA* driver (n=6 flies). Middle: fictive odor (*Orco-LexA*, n=9). Right: fictive heat (*Gr28b.d-LexA*, n=9 flies). Plots show mean ±SEM across flies. Note that behavioral responses are larger and less variable in these intact flies. The reduced behavioral performance of the flies in Fig. 1 is likely due to local removal of the peri-neural sheath and/or local disruption of the neuropil surrounding a2 somata during the patching procedure. Nonetheless, the qualitative features of behavior in Fig. 1 are comparable to intact flies.

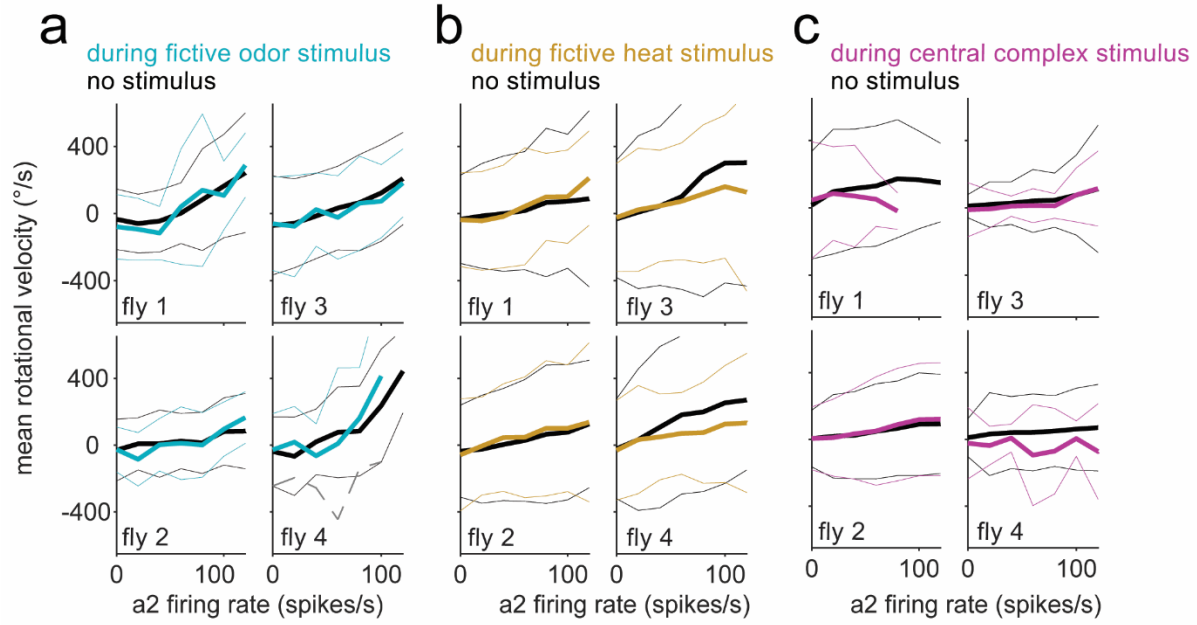

Supplementary Figure 2: Comparing neuron/behavior curves during stimulus-evoked steering and spontaneous steering

a, In each fictive odor experiment (Fig. 1), we measured rotational velocity and a2 firing rate in 50-ms time windows. We separated windows when the stimulus was present from windows when the stimulus was absent. Both ipsi- and contralateral stimulus periods were included. We then binned the data by firing rate and averaged rotational velocity values within each bin (thick line). Thin lines show 95% confidence intervals around the mean. Each panel is a different fly. Most of these plots show a mean relationship between rotational velocity and firing rate that is similar to the linear fits in Figs. 1f and 3g; in those plots a firing rate increase of ~100 spikes/s produces an increase in ipsilateral rotational velocity of ~100º/s.

b, Same but for fictive heat experiments.

c, Same but for central complex stimulation experiments. Here, the "stimulus" epoch is defined as the 750 ms window prior to the maximum bump return speed. A few of these plots show a shallower slope (e.g., flies 2 and 3), possibly because these flies were in a different behavioral state.

Note that the neuron-behavior curve is similar in the two conditions in each experiment. This implies that a2 has the same quantitative relationship to steering behavior, regardless of whether steering is evoked by an olfactory stimulus, a thermal stimulus, a compass steering drive, or a spontaneous steering drive.

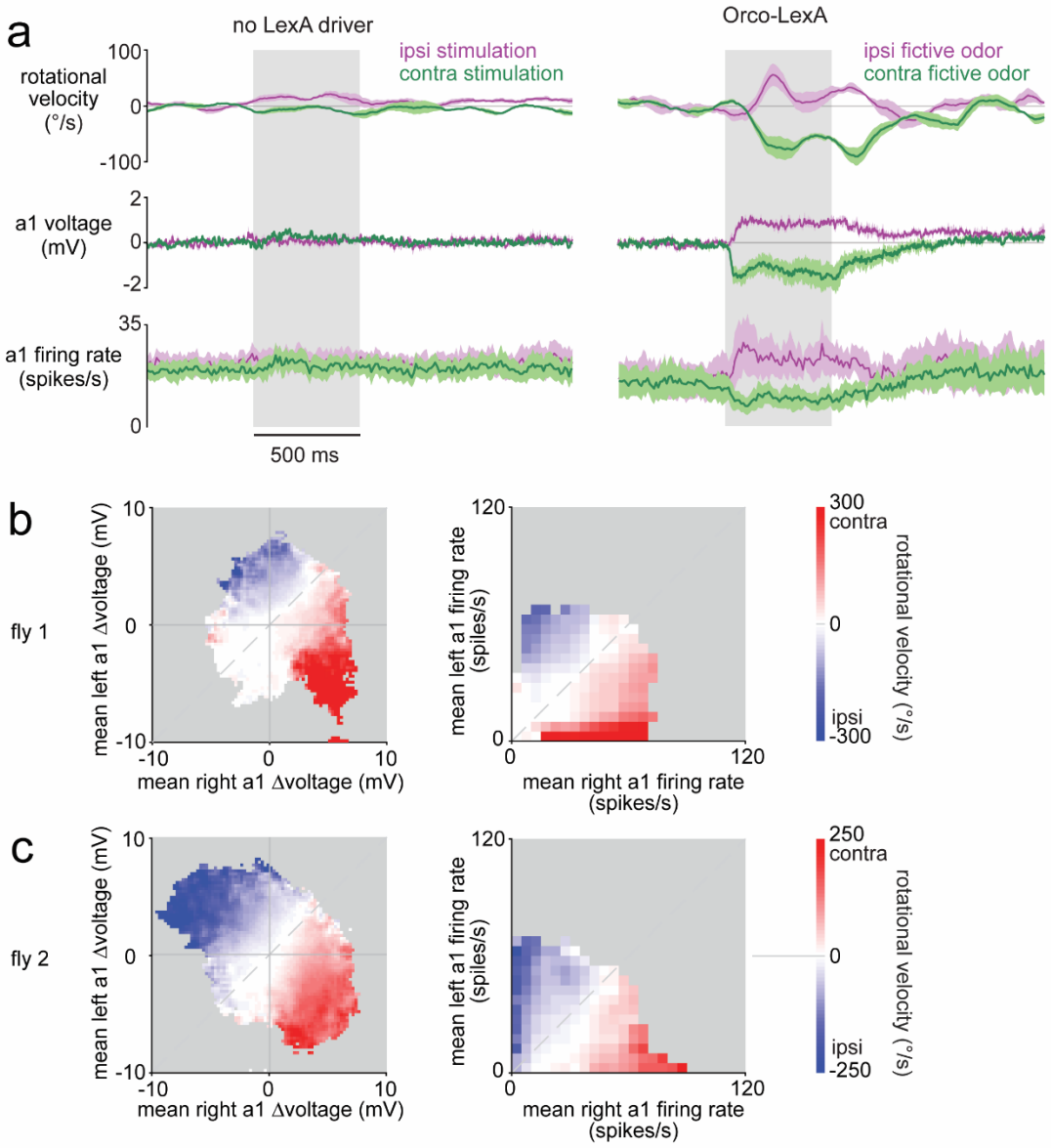

Supplementary Figure 3: Steering correlations of a1 neurons

a, Rotational velocity and a1 activity during fictive odor presentations. Each plot shows mean ± SEM across flies (n=4 genetic controls with no LexA driver, n=3 flies harboring *Orco-LexA*). On average, a1 activity is weaker than a2 activity during odor-evoked turning behavior (Fig. 1), but qualitatively a1 and a2 have similar relationships to odor-evoked turning.

b, An example paired a1/a1 recording. Colormap shows binned and averaged rotational velocity for each value of bilateral a1 Δvoltage (left) and bilateral a1 firing rates (right). Note that rotational velocity is related to the right-left firing rate difference in this a1 paired recording. This is similar to our results in a2 paired recordings (Fig. 7b-d).

c, Same but for another example paired a1/a1 recording.

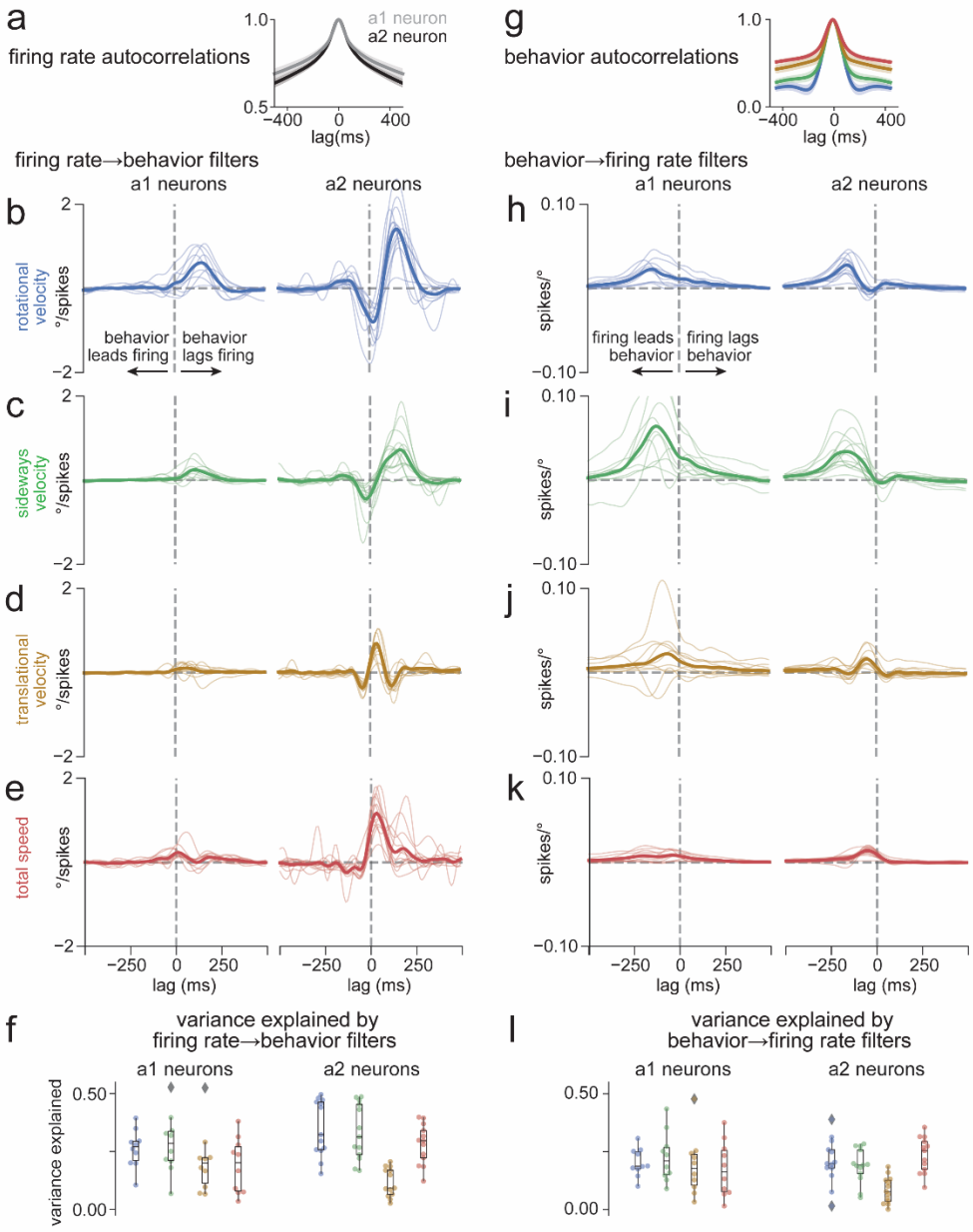

Supplementary Figure 4: Forward and reverse linear filters for a1 and a2 neurons

a, Firing rate autocorrelation for a1 and a2 neurons.

b, Firing-rate-to-rotational-velocity filters (f→r), for a1 neurons and a2 neurons.

c, Firing-rate-to-sideways-velocity filters (f→s), for a1 neurons and a2 neurons.

d, Firing-rate-to-translational-velocity filters (f→t), for a1 neurons and a2 neurons.

e, Firing-rate-to-total-speed filters (f→total speed), for a1 neurons and a2 neurons. Recall that total speed $= |r| + |s| + |t|$. Because a2 predicts large changes in r and s, it is not surprising that it is also predicts large changes in total speed. The filters in (b-e) can be convolved with neural firing rates to predict behavior: b(t) = H(t) * f(t). The filters in (b-d) are reproduced from Fig. 5.

f, Variance explained by each forward filter, for each kinematic variable, for a1 and a2 neurons. Colors correspond to (b-e).

g, Behavior autocorrelation for each kinematic variable. Colors correspond to (b-e).

(**h-k**) Same as in (b-e), but in the reverse direction (r→f, s→f, etc.). These filters can be convolved with a behavioral variable to predict neural firing rates: f(t) = H(t) * b(t). Whereas the forward filters in (b-e) are normalized for the neuron's autocorrelation function, these reverse filters are normalized for behavior autocorrelation.

l, Variance explained by each reverse filter, for each kinematic variable, for a1 and a2 neurons.

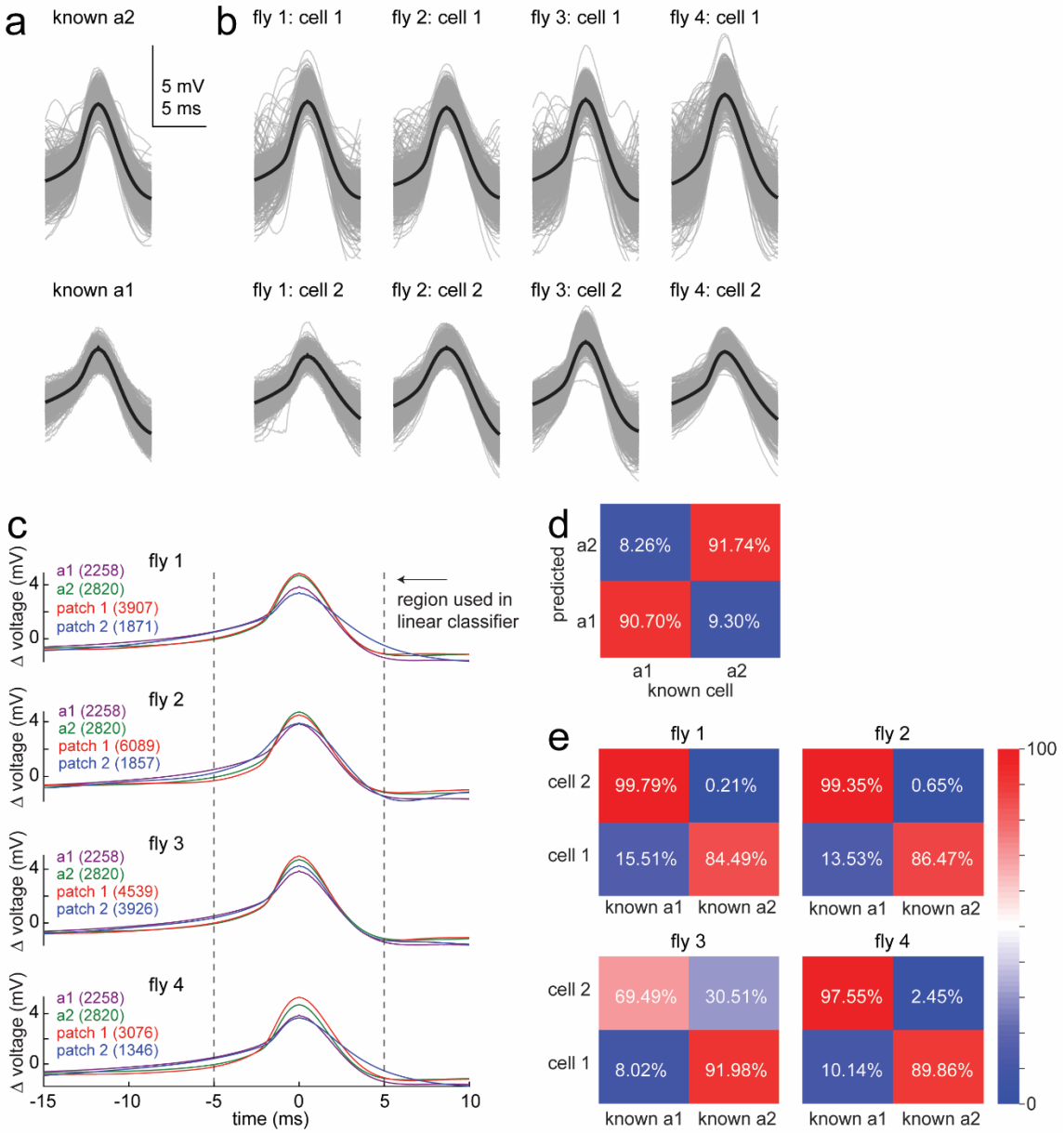

Supplementary Figure 5: Spike waveform analysis during dual a1/a2 recording

a, Top: spike waveforms from a known a2 cell, recorded in the specific split-Gal4 line (SS00730). Bottom: spike waveforms from a known a1 cell, recorded in a different specific split-Gal4 line (SS00731). Individual spikes are gray, averages in black.

b, Spike waveforms from dual a1/a2 recordings in 4 flies.

c, Magenta and green lines show overlaid averages from (a). Red and blue show overlaid averages from (b). Dashed lines show the part of the waveform used in classification analysis. Values in parentheses show the number of spikes in each average.

d, A linear classifier was trained to separate cells from known a1 and a2 recordings, using the data shown in (A). In essence, the classifier separates spike waveforms based on their shapes and amplitudes. This classifier was then tested using another pair of known a1 and a2 recordings. Values shown are the percentage of spikes assigned to each cell type. Because most of the a1 spikes were assigned to the a1 category, and most of the a2 spikes were assigned to the a2 category, we can conclude that this classifier produces the correct identification of the two cells.

e, The same classifier was then applied to dual a1/a2 recordings from all 4 flies, in order to determine which cell was which. In every case, the classification was essentially unambiguous. Moreover, in every case, the classifier assigned the a1 label to the cell with the smaller and deeper soma, consistent with our observation that the soma of a1 is somewhat smaller and deeper than the soma of a2.

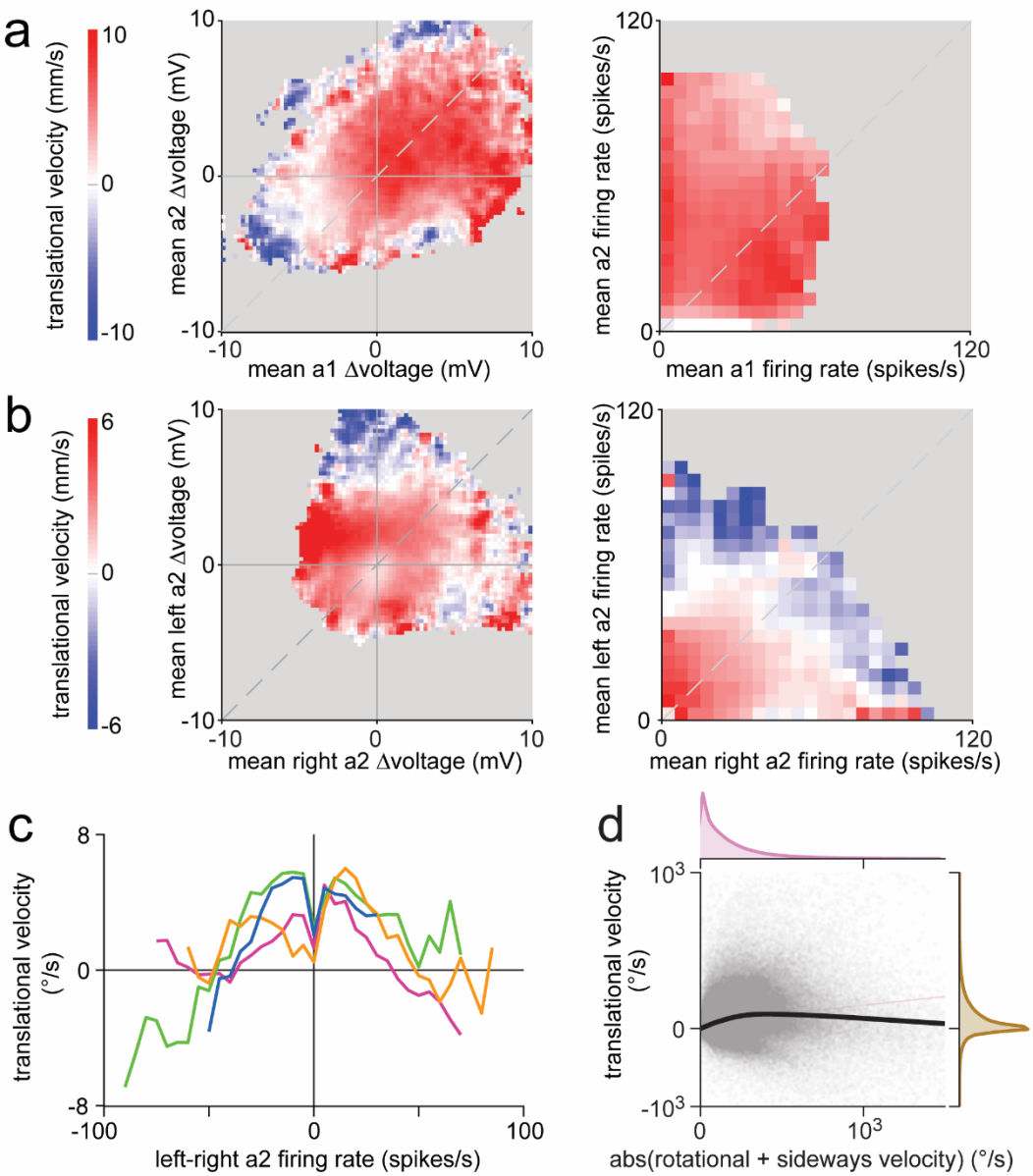

Supplementary Figure 6: Translational velocity and neural activity in paired recordings

a, From an example a1/a2 paired recording, colormaps show binned and averaged translational velocity for each paired value of Δvoltage (left) or firing rate (right). Both a1 and a2 were recorded in the left hemisphere. When ($\Delta voltage_{a2} >> \Delta voltage_{a1}$), the fly is typically moving backward. When (firing $rate_{a2}$>>firing $rate_{a1}$), the fly is also often moving backward, but forward movement is still more common overall, and so the net effect is that translational velocity is small but still positive when (firing $rate_{a2}$>>firing $rate_{a1}$). Note that when we condition our analysis on behavior rather than neural activity, we do see that backward walking is associated with a large firing rate differential (Supplementary Fig. 7c).

b, From an example a2/a2 paired recording, colormaps show binned and averaged translational velocity for each paired value of Δvoltage (left) or firing rate (right). When both left and right a2 cells are firing zero spikes, the fly is typically stopped (see also Fig. 2). When either copy of a2 is firing at a high rate, the fly is often moving backward; this is likely because extremely fast turns are often associated with backward movement.

c, Mean translational velocity for each left-right a2 firing rate difference. Each line is a different fly (n=4). Large left-right differences are associated with backward movement; again, this is likely because extremely fast turns are often associated with backward movement.

d, Translational velocity versus steering speed (defined as the absolute value of rotational velocity plus sideways velocity, both in units of °/s). Black line is a LOWESS fit to the full scatter plot of the relationship in 20 flies. Margins show kernel density estimates. Note that, in the regime of typical steering speeds (<500 °/s), increasing steering speed is associated with increasing translational velocity. However, for very fast steering speeds, increasing steering speed is associated with decreasing translational velocity, partly because there are more instances of backward movement.

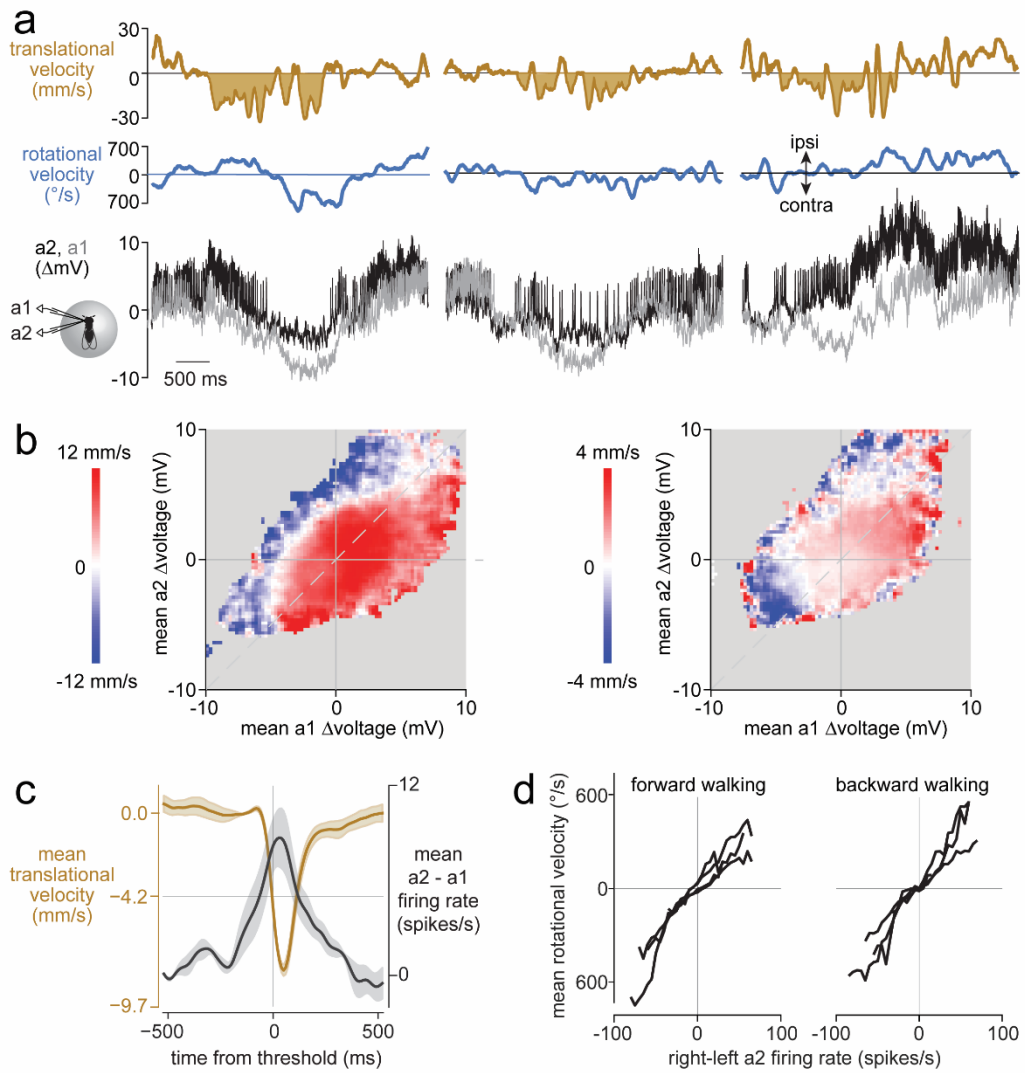

Supplementary Figure 7: Backward walking

a, Three examples of dual recordings from a1 and a2. When a2 is much less hyperpolarized than a1 (or much more depolarized), the fly is generally moving backward. Flies typically moved backward ~15% of the time.

b, Colormap shows binned and averaged translational velocity for each value of a1 and a2 membrane voltage, for three example paired recordings. Voltages are expressed as changes from each cell's mean.

c, Mean difference in firing rates (a2-a1), ± SEM across flies (n=4 flies), aligned to the onset of backward walking. Overlaid is mean translational velocity ± SEM across flies; horizontal line represents the threshold used to trigger onset of backward walking.

d, Binned and averaged rotational velocity versus bilateral firing rate difference for epochs of forward walking and backward walking. Each line is a different paired recording (n=4 flies).

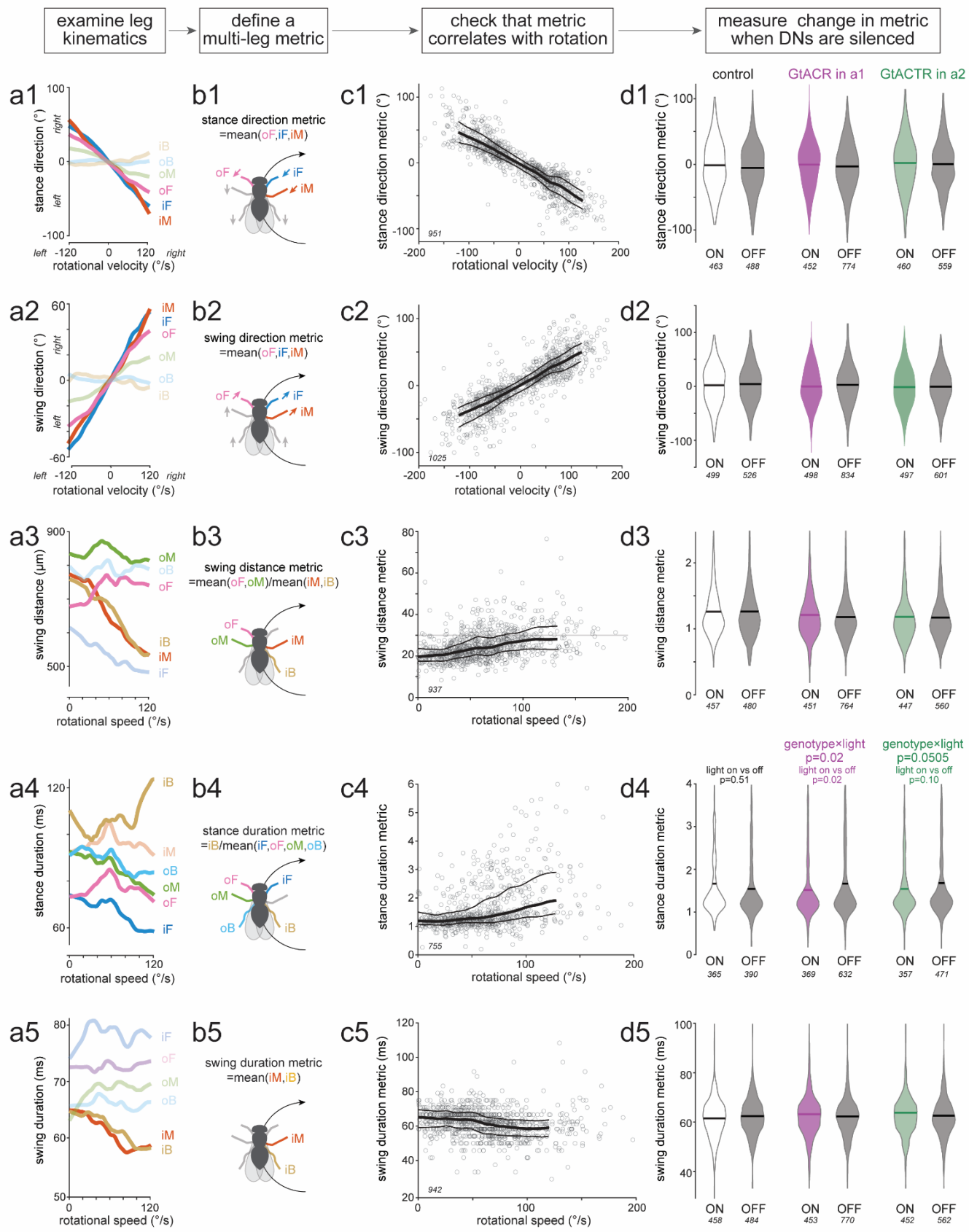

Supplementary Figure 8: Leg movements associated with body rotation

a, We selected 5 leg-kinematic variables likely to be associated with body rotation. In control flies, we computed the mean value of each variable, for each leg, binned by rotational velocity (for directional variables) or rotational speed (for nondirectional variables).

b, We defined 5 multi-leg metrics, each based on one leg-kinematic variable. For each metric, the relevant legs are labeled and color-coded. Gray legs were not used because, for these legs, the variable in question did not show a reliable correlation with the fly's rotational movement (a). Gray legs in (b) are shown in faded colors in (a).

c, Next, we plotted each metric versus rotational velocity or rotational speed, to verify that the expected relationship was observed. We refined our definitions in order to optimize the signal-to-noise ratio of this relationship. Each datapoint is a time window (with n values in italics near the origin of each plot). Thick lines show LOWESS fits; thin lines show 95% confidence intervals; only a small number of datapoints have rotational speeds >120º/s, so fits are not shown above this ceiling. Importantly, we fixed the number of metrics we tested, and also the definitions of those metrics, based purely on data from control flies, before we examined any of these metrics in our experimental genotypes.

d, Finally, we asked how these metrics change when a1 or a2 neurons are silenced. We identified all body rotation events in every experiment by searching forward in time for moments when rotational speed crosses a threshold of 20 º/s. We extracted a 500-ms time window around each threshold-crossing. Events were constrained to be non-overlapping. Body rotation events were tabulated separately for light-on and light-off. The number of time windows in each distribution is shown in italics. To determine if any metric was changed when a1 neurons were silenced, we performed 5 two-factor ANOVAs and looked for a significant interaction between genotype (control/a1) and light (on/off); these p-values were Bonferroni-Holm corrected to avoid type 1 errors (m=5 tests). Then, to determine if any metric was changed when a2 neurons were silenced, we performed 5 two-factor ANOVAs and looked for a significant interaction between genotype (control/a2) and light (on/off); these p-values were again Bonferroni-Holm corrected (m=5 tests); nonsignificant p-values are not shown. Then, in cases where these p-values were significant (**d4**, p=0.02, a1 vs control) or nearly significant (**d4**, p=0.505, a2 vs control), we followed up by performing a post hoc Tukey test to determine if there was a significant difference between light on/off in each genotype. Interestingly, the only metric to show an effect was the stance duration metric (**d4**). In control flies, a prolonged stance duration is observed in some but not all body rotation events (**c4**). This implies that body rotation can be driven by an inner-back-leg pivoting maneuver, but body rotation does not absolutely require this maneuver. This idea is consistent with our finding that rotational speeds are overall unchanged when a1 or a2 is silenced (Fig. 8e).

Note that the data for the stance duration metric (**a4-d4**) are reproduced in Fig. 8f,g, where this metric is called "inner back leg stance duration (normalized)", i.e. iB pivoting.

Supplementary Table 1: Neurons presynaptic to a2 reconstructed from the full-brain EM volume.

Neuron Name	Synapses per Connection	Neuron from Figure 4
PFL3_1	15	4d (1)
PFL3_2	20	4d (2)
PFL3_3	10	4d (3)
PFL3_4	17	4d (4)
PFL3_5	20	4d (5)
PFL3_6	19	4d (6)
PFL3_7	16	4d (7)
PFL3_8	17	4d (8)
PFL3_9	9	4d (9)
PFL3_10	9	4d (10)
PFL3_11	27	4d (11)
PFL3_12	20	4d (12)
AOTUtoL_1	17	4e, green
AOTUtoL_2	37	4e, blue
AOTUtoL_3	10	4e, orange
AOTUtoL_4	4	4e, magenta
LC9_1	4	4f, green
LC9_2	5	4f, orange
SMPtoL1_1	6	4g, green
SMPtoL1_2	3	4g, blue
SMPtoL2_1	58	4g, orange
SMPtoL2_2	19	4g, magenta
AVLPtoL1_1	8	4h, green
AVLPtoL1_2	20	4h, orange
LtoL1_1	32	4i, green
LtoL1_2	41	4i, orange
DN_1	172	4j, green
DN_2	124	4j, orange

ONLINE METHODS

Fly husbandry and genotypes

We used female flies 1-2 days post-eclosion, except where specified below. We used virgins to minimize egg-laying, which tended to stop movement of the spherical treadmill. Flies were housed in a 25° incubator at 50-70% humidity. Unless otherwise noted, flies were cultured on molasses food (B7 recipe, Archon Scientific) and kept on a 12/12 light/dark cycle. The split-Gal4 lines[53] targeting DNs[14] were *SS00730* for a2 (*R75C10-p65ADZp* in *attP40*; *R87D07-ZpGdbd* in *attP2*) and *SS00731* for a1 (*R22C05-p65ADZp* in *attP40; R56G08-ZpGdbd* in *attP2*); these were obtained from Gwyneth Card (Janelia Research Campus). Each of these split-Gal4 lines typically drives expression in one cell per brain hemiphere, although *SS00731* occasionally drives expression in two cells per hemisphere. *R75C10-Gal4(attP2)*[54,55] and *R60D05-LexA(attP40)*[53] were obtained from the Bloomington Drosophila Stock Center (BDSC). *VT032906-Gal4(attP2)*[56] was obtained from the Vienna Drosophila Resource Center. *Orco-LexA* (on chromosome 3)[56] was obtained from Tzumin Lee (Janelia Research Campus). *Gr28b.d-LexA* (on chromosome 2) was obtained from Marco Gallio (Northwestern University)[57]. *hsFLP.122*[58-60] was obtained from Thomas Clandinin (Stanford University). *UAS-GtACR1::eYFP(VK00005)* was obtained from Michael Crickmore (Boston Children's Hospital); this reagent has not been published previously. *pJFRC81-td3-Halo7::CAAX(attp18)* was obtained from Greg Jefferis via Luke Lavis; this specific reagent has not been published previously, although general methods its construction have been published[61]. *UAS-P2X2* (chromosome 3)[35] was obtained from Gero Miesenböck (Oxford University). Finally, the following stocks were obtained from the BDSC: *10XUAS-IVS-mCD8::GFP(su(Hw)attP8)*[53], *10XUAS-IVS-mCD8::GFP(attP40)*[53], *UAS(FRT.mCherry)ReaChR(VK00005)*[62], *p65.AD.Uw(attP40); GAL4.DBD.Uw(attP2)*[63], *13XLexAop2-IVS-GCaMP6f-p10(su(Hw)attP5)*[64], *13XLexAop2-IVS-CsChrimson::mVenus(attP40)*[65], *13XLexAop2-IVS-CsChrimson::mVenus(attP18)*[65], *13XLexAop2-IVS-CsChrimson::mVenus(attP2)*[65].

Genotypes of fly stocks used in each figure are as follows:

*a2 single/dual recording (*Figs. 2c,d, 5b-f, 7; Supplementary Figs. 4a-g,l, 6b,c, 7d)
y^1, w, 10XUAS-IVS-mCD8::GFP(su(Hw)attP8) / w; R75C10-p65ADZp (attP40) / +; R87D07-ZpGdbd (attP2) / +
and
w^{1118},13XLexAop2-IVS-CsChrimson::mVenus(attP18) / w; 10XUAS-IVS-mCD8::GFP(attP40) / R75C10-P65ADZP(attP40); Orco-LexA / R87D07-ZpGdbd(attP2)

a1 single/dual recording (Fig. 5c-f; Supplementary Figs. 3b,c, 4f,h-l)
y^1, w, 10XUAS-IVS-mCD8::GFP(su(Hw)attP8) / w; R22C05-p65ADZp(attP40) / +; R56G08-ZpGdbd(attP2) / +

a1/a2 dual recording (Fig. 6; Supplementary Figs. 4, 5, 6a, 7a-c)
y^1, w, 10XUAS-IVS-mCD8::GFP(su(Hw)attP8) / w; R22C05-p65ADZp(attP40) / 10XUAS-IVS-mCD8::GFP(attP40); R56G08-ZpGdbd(attP2) / R75C10-GAL4(attP2)

fictive odor with a2 recording (Figs. 1b,e,g, 2a,b; Supplementary Figs. 1b, 2a)
w^{1118},13XLexAop2-IVS-CsChrimson::mVenus(attP18) / w; 10XUAS-IVS-mCD8::GFP(attP40) / R75C10-P65ADZP(attP40); Orco-LexA / R87D07-ZpGdbd(attP2)

fictive heat with a2 recording (Fig. 1f; Supplementary Figs. 1b, 2b)
y^1, w, 10XUAS-IVS-mCD8::GFP(su(Hw)attP8) / w; R75C10-P65ADZP(attP40) / Gr28b.d-LexA; R87D07-ZpGdbd(attP2) / 13XLexAop2-IVS-CsChrimson::mVenus(attP2)

fictive odor with a1 recording (Supplementary Fig. 3a)
y^1, w, 10XUAS-IVS-mCD8::GFP(su(Hw)attP8) / w; R22C05-p65ADZp(attP40) / Orco-LexA; R56G08-ZpGdbd(attP2) / 13XLexAop2-IVS-CsChrimson::mVenus(attP2)

no-LexA control for fictive odor and fictive heat, a2 recordings (Supplementary Fig. 1)
y^1, w, 10XUAS-IVS-mCD8::GFP(su(Hw)attP8) / w; R75C10-P65ADZP(attP40) / +; R87D07-ZpGdbd(attP2) / 13XLexAop2-IVS-CsChrimson::mVenus(attP2)

no-LexA control for fictive odor and fictive heat, a1 recordings (Supplementary Fig. 3a)
y^1, w, 10XUAS-IVS-mCD8::GFP(su(Hw)attP8) / w; R22C05-p65ADZp(attP40) / +; R56G08-ZpGdbd(attP2) / 13XLexAop2-IVS-CsChrimson::mVenus(attP2)

calcium imaging and a2 recording during central complex stimulation (Fig. 3; Supplementary Fig. 2c)
w, pJFRC81-td3-Halo7::CAAX(attP18) / w; R75C10-P65ADZP(attP40) / R60D05-LexA(attP40), 13XLexAop2-IVS-GCaMP6f-p10(su(Hw)attP5); R87D07-ZpGdbd(attP2) / UAS-P2X2, VT032906-Gal4(attP2)

central complex-evoked turning, control (Fig. 3b)
w, pJFRC81-td3-Halo7::CAAX(attP18) / w; R75C10-P65ADZP(attP40) / R60D05-LexA(attP40), 13XLexAop2-IVS-GCaMP6f-p10(su(Hw)attP5); R87D07-ZpGdbd(attP2) / UAS-P2X2

Unilateral direct optogenetic activation of a2 (Fig. 8a-c)
y, w, hsFLP.122 / w; R75C10-P65ADZP(attP40) / +; R87D07-ZpGdbd(attP2) / UAS-FRT.mCherry.FRT.ReachR(VK00005)

Bilateral optogenetic silencing of a1 (Fig. 8d-h, Supplementary Fig. 8)
w; R22C05-p65ADZp(attP40) / +; R56G08-ZpGdbd(attP2) / UAS-GtACR1::eYFP(VK00005)

Bilateral optogenetic silencing of a2 (Fig. 8d-h, Supplementary Fig. 8)
w; R75C10-P65ADZP(attP40) / +; R87D07-ZpGdbd(attP2) / UAS-GtACR1::eYFP(VK00005)

Control for optogenetic silencing ("empty" split-Gal4) (Fig. 8d-h, Supplementary Fig. 8)
w; p65.AD.Uw(attP40) / +; GAL4.DBD.Uw(attP2) / UAS-GtACR1::eYFP(VK00005)

Fly mounting and dissection for electrophysiology and calcium imaging

On the day of the experiment, a fly was cold-anesthetized and then inserted into a hole in a stainless-steel, machine milled platform (Harvard Medical School Research Instrumentation Core). We secured the fly to the platform using UV-curable glue (AA3972 Loctite) applied on the thorax and eyes.

We then extended the proboscis with forceps and waxed it in place to prevent brain motion (Electra Waxer, Almore); prior to this step, a manual manipulator (MX160R Siskiyou) was used to lower a shield over the legs to protect them from the tip of the waxer. We then covered the brain with extracellular saline composed of: 103 mM NaCl, 3 mM KCl, 5 mM TES, 8 mM trehalose, 10 mM glucose, 26 mM $NaHCO_3$, 1 mM NaH_2PO4, 1.5 mM $CaCl_2$, and 4 mM $MgCl_2$ (osmolarity 270-275 mOsm). The saline was bubbled during the dissection with 95% O_2 and 5% CO_2 and reached an equilibrium pH of 7.3. The top of the cuticle was removed, followed by air sacs and fat globules around the patching site. Muscle 16 was severed to prevent brain motion. The frontal head air sac, which extends ventrally under the brain, was also removed to improve illumination from below the brain. Finally, we mechanically removed the peri-neural sheath over the patching site. (For behavior-only experiments in Fig. 8 and Supplementary Fig. 1b, all these dissection steps were omitted.)

Finally, we transferred the fly to the spherical treadmill, where we used a motorized three-axis manipulator (MT3-Z8, Thorlabs) to adjust the fly relative to the ball. Two cameras (BFLY-PGE-13E4M, FLIR) were used to visualize the fly during this adjustment.

Spherical treadmill and behavioral measurements

We used a sensor-based setup for tracking the movements of the spherical treadmill[66]. Briefly, a hollow HDPE sphere (6.35 mm diameter) was floated on pressurized air, in a plenum mounted on a manipulator to allow alignment of the center of the ball with two motion sensors located at a distance from the ball. The ball was painted with a random dot pattern to make it easier for motion sensors to detect movement. We positioned two cameras 90° apart to track the motion of the ball in three dimensions (rotational, sideways, translational velocity), and we took the fly's fictive movements in each direction as equal and opposite to the ball's movements. These motion cameras were custom built by housing the motion sensor array (ADNS-9800, JACK Enterprises) in a custom housing with a lens (M2514-MP2, Computar). Data from the sensor was read out and translated into an analog signal using a digital-to-analog converter (MCP4725, SparkFun) and an Arduino device (Due, Arduino). Analog data were digitized at 10 kHz with a multi-channel NI DAQ board (PCIe-6353, National Instruments), controlled via the Matlab Data Acquisition Toolbox interface (MathWorks). Analog data were then smoothed using a 2nd-order lowpass Butterworth filter and downsampled to 100 Hz.

Motion sensor outputs were calibrated to obtain the conversion from sensor outputs to ball velocities. We performed this calibration by rotating a ball using a planetary gear motor with an encoder (Actobotics, Part 3638298). The motor was rotated at 6 different speeds in all 3 axes of motion, and linear regression was used to calculate the mapping between the output of the motion sensors and the rotation of the ball.

We noticed that steering responses to sensory stimuli were larger and more consistent in intact flies, as compared to flies used for electrophysiology experiments (Supplementary Fig. 1b). The reduced performance of flies used for electrophysiology experiments is likely due to local removal of the peri-neural sheath and/or local disruption of the neuropil surrounding the targeted somata. Nonetheless, the qualitative features of behavior are comparable in intact flies and flies used for electrophysiology (Fig. 1 and Supplementary Fig. 1b).

Electrophysiology

For patch clamp experiments, we illuminated the brain with an infrared fiber (SXF30-850, Smart Vision Lights) mounted under the fly tethering platform in a sagittal plane at ~20° from the horizontal and a we visualized the brain with a camera (BFLY-PGE-13E4M, Point Gray) mounted on a fluorescence microscope (BX51, Olympus).

Before attempting to obtain seals, we first used a large-diameter glass pipette filled with extracellular saline (4-5 MΩ), to clear the area around the soma of interest by applying positive pressure and also gently sucking away any cells lying on top of the soma of interest. Patch pipettes (9-11 MΩ) were pulled the day of the recording and filled with internal solution containing 140 mM KOH, 140 mM aspartic acid, 10 mM HEPES, 1 mM EGTA, 1 mM KCl, 4 mM MgATP, 0.5 mM Na_3GTP, and 13 mM biocytin hydrazide (pH adjusted to 7.2 ± 0.1, osmolarity adjusted to 265 ± 3 mOsm). Whole-cell patch-clamp recordings were performed from fluorescently labeled somata in current-clamp mode using an Axopatch 200B amplifier. Data were low-pass filtered at 5 kHz, digitized at 10 kHz by a 16 bit A/D converter (National Instruments, BNC 2090-A), and acquired using the Matlab Data Acquisition Toolbox (MathWorks). Recordings were stable for at least 15 min and up to 2 hrs.

We always recorded from the neuron in the left hemisphere, except when we recorded from the same cell type bilaterally. For bilateral recordings, we performed the cleaning and air-sac clearing steps on both sides of the brain. For dual recording experiments of a1 and a2, we performed recordings on the left side of the brain.

We targeted a1 using *SS00731*, and we targeted a2 using *SS00730*[14]; the only exception was that, in dual a1 and a2 recordings, we targeted a1 using the *SS00731*, and we targeted a2 using *R75C10-Gal4*. In these flies, we could identify a1 and a2 based on the depths of their somata (a2 is more superficial), the sizes of their somata (a2 is larger), and their spike waveforms (a2 spikes are larger). Finally, to confirm the discriminability of a2 and a1 spikes, we quantified the performance of automated spike waveform classification (Supplementary Fig. 5).

Fictive odor and fictive heat stimuli

Flies for the experiments in Figs. 1 and 2 (and Supplementary Figs. 1, 2a,b, and 3a) were cultured on molasses food (see above) and then transferred 0-1 days after eclosion onto a vial of standard cornmeal agar fly food supplemented with rehydrated potato flakes (Formula 4-24, Carolina Biological Supply) and 100 µL of all-*trans*-retinal (35 mM in ethanol; R2500, Sigma-Aldrich). These vials were covered with aluminum foil to prevent photoconversion of all-*trans*-retinal by ambient light. In these flies, we used the LexA system to express *LexAOp-CsChrimson::mVenus* under the control of either *Orco-LexA*[56] or *Gr28b.d-LexA*[57]. To illuminate the antennae, we fixed a pair of 50-µm fiber optic cannulas (10 mm long, FG050UGA, Thorlabs) to the underside of the recording platform, so that each fiber was directed at one antenna. Alignment of each cannula was confirmed in every experiment by looking for uniform and symmetric illumination of each antenna[28]. A 660 nm light source was fiber-coupled to each cannula (M660F1, Thorlabs). Stimulation lasted for 0.5 s, with an inter-stimulus interval of 11 s.

Calcium imaging and electrophysiology during central complex stimulation

In the experiments for Fig. 3 (and Supplementary Fig. 2c), the pitch angle of fly's head was carefully adjusted during the dissection procedure. This allowed patch-pipette access to the anterior side of the brain (where a2 somata reside) as well as pressure-pipette access to the protocerebral bridge on the posterior side of the brain (where P-EN1 dendrites reside).

To position the pressure-ejection pipette in the protocerebral bridge, and to obtain a patch recording from an a2 somata, we visualized the brain and the patch pipette using an infrared fiber (SXF30-850, Smart Vision Lights) mounted under the tethering platform in a sagittal plane at ~20° from the horizontal and a near-infrared camera (GS-U3-41C6NIR FLIR) mounted on the widefield viewing port of a 2-photon microscope (Bergamo II, Thorlabs).

To obtain a recording from a2, we needed to fluorescently label a2 somata. However, we needed to label a2 without also labeling P-EN1 neurons (which also expressed Gal4), because P-EN1 labeling could have contaminated our GCaMP6f signal in the ellipsoid body. We therefore used a chemogenetic approach[61]. Specifically, we drove expression of HaloTag under *Gal4*/*UAS* control, and we then applied SiR110-HaloTag dye[67] (a gift from Luke Lavis) to the preparation. The dye was prepared as a stock solution (500 µM in DMSO), and then 1 µL of the stock was dissolved in 500 µL of extracellular saline. Most of the saline in the recording chamber was removed and the dye solution was added to the chamber. After a 15 min incubation, the chamber was rinsed and re-filled with regular extracellular saline. We used a TexasRed filter cube (49017, Chroma) to visualize labeled a2 somata. Because the perineural sheath was removed selectively in the vicinity of a2 somata, the bath-applied SiR110-HaloTag dye bound mainly to a2 somata, with essentially no binding to the ellipsoid body neuropil.

For GCaMP6f imaging of E-PG neuron dendrites in the ellipsoid body, we used a volumetric, galvo-resonant scanning 2-photon microscope (Bergamo II, Thorlabs) equipped with a 20×, 1.0 n.a. objective (XLUMPLFLN20XW, Olympus) and GaAsP detectors (Hamamatsu). We used ScanImage 2018 software (Vidrio Technologies) to control the microscope. Two-photon excitation was provided by a Chameleon Ultra II

Ti:Sapphire femtosecond pulsed laser with pre-compensation (Vision-S, Coherent). To image GCaMP6f, we tuned the laser to 940 nm. The objective was translated vertically using a scanner with a 400-µm travel range (P-725KHDS PIFOC, Physik Instrumente). The ellipsoid body was volumetrically imaged with 12 *z*-planes of 256×64 pixels separated by 4-5 µm. We acquired ~12 volumes/s.

For P-EN1 stimulation, we followed a published procedure[10]. We prepared a solution of ATP (A7699, Sigma, 0.5 mM) and Alexa594 dye (A33082, FisherScientific, 20 µM,) in extracellular saline. This solution was used to fill a glass pipette slightly smaller than a patch pipette. We used a red emission filter cube (49017, Chroma) to visually locate the pipette via the microscope eye pieces. The tip of the pipette was placed into the protocerebral bridge, where the dendrites of P-EN1 neurons are located, generally close to glomerulus 4[33]. To eject ATP and dye, we delivered a 50-100 ms pulse of pressure to the back of the pipette (10-20 p.s.i.) using a pneumatic device gated by a voltage pulse (PV820; World Precision Instruments). We confirmed ejection by observing a bolus of dye appear in the center of the protocerebral bridge neuropil, and the resulting stimulus-locked rotation of the E-PG bump in the ellipsoid body.

In a given experiment, we noticed that the bump tended to jump to the same location in every trial. We used that fact to try to obtain large bump jumps. Specifically, we manually timed the ATP injection in each trial to maximize the size of the resulting bump jump. We ejected ATP every 15-25 s for a total of 87 ± 10 stimulations per fly.

As a negative control, we performed the same type of experiment in flies lacking the P-EN1 Gal4 line, and we confirmed that the ATP puff only rarely preceded bump jumps in this genotype (Fig. 3b). This negative result demonstrates that the bump jump in the experimental genotype is primarily driven by P2X2 expression in P-EN1 neurons. Bump jumps in control flies are likely coincidental, as the bump is often moving in a typical E-PG imaging experiment. In control flies, in the few trials where the bump jumped, the bump returned to its initial location 35% of the time. These returns are not unexpected, because the bump's location is thought to be continuously compared to an internal goal location stored downstream from E-PG neurons, and any deviation from the fly's angular goal is corrected via compensatory turning maneuvers.

Note that, in these experiments, E-PG neurons expressed GCaMP6f (under the control of *60D05-LexA*), P-EN1 neurons expressed $P2X_2$ and HaloTag (under the control of *VT032906-Gal4*), and a2 neurons also expressed $P2X_2$ and HaloTag (under the control of *SS00730*). We took several steps to verify that ATP directly stimulated P-EN1 neurons but not a2 neurons. First, we used dye to check that the ATP bolus was confined to the protocerebral bridge. Second, we confirmed that a2 neurons were not depolarized during the period when P-EN1 neurons were depolarized and the bump therefore jumped, i.e. in the first 0.5 s after ATP ejection (mean a2 voltage change in the 0.5 s after ATP ejection was 0.12 ± 0.27 mV in experimental flies and 0.14 ± 0.27 mV in genetic controls lacking the P-EN1 Gal4 driver). Rather, a2 neurons were only excited just before the fly made a compensatory steering maneuver, which usually occurred 1.0-1.5 s after the bump jump. Third, we verified that a2 was only recruited when the bump returned to its initial location via a clockwise path; if ATP had been directly exciting a2, then the side where a2 was active should not be contingent on the bump's path.

EM reconstruction

Identifying a2. We traced neurons in the female adult fly brain (FAFB) dataset[36], using the CATMAID toolkit[68]. To identify a2, we began by tracing all the neurites with large cross-sections in the tract where a2's primary neurite resides, in the vicinity of the ventral LAL. All these primary neurites were reviewed by two experts, who agreed that only one neuron resembled a2. We then fully reconstructed the skeleton of this a2-like neuron. Next, we confirmed that this neuron bore an excellent resemblance to skeletons we traced from two 3D confocal images of the a2-specific split-Gal4 line (*SS00730*) driving CD8::GFP expression (Fig. 4a). The first of these images was provided to us by Gwyneth Card[14]. The second image we obtained independently, via immunostaining and confocal imaging using standard procedures. We registered both 3D images to a common

template brain[69] (JFRC2013) using the neuropil counterstain (anti-Bruchpilot immunostaining). Image registration was carried out as described previously[70] using the CMTK registration suite (https://www.nitrc.org/projects/cmtk). Single neurons were manually traced from 3D confocal images using the Simple Neurite Tracer plugin[71] in ImageJ. For comparison with light-level data, the EM skeleton was also registered onto the JFRC2013 template brain.

Inputs to a2. Once we identified a2 in the FAFB dataset, we annotated all the presynaptic sites (1,497) and postsynaptic sites (10,842) within the brain domain of this neuron. We then partially reconstructed the skeletons of 658 neurons presynaptic to a2 and 25 neurons postsynaptic to a2. Finally, we selected 28 presynaptic neurons for complete skeletonization. Each of these 28 neurons has been reconstructed by one expert and independently reviewed by a second expert.

Analysis of EM data. Analyses of FAFB skeletons and synapses were performed in R using open-source software. RCatmaid[69] was used to interface with CATMAID servers. All other neuron analyses and visualizations were performed with natverse[69] functionality or custom-written code. Synapses and connected skeletons were retrieved from CATMAID using catnat (https://jefferislab.github.io/catnat/). In order to group synapses by brain region (Fig. 4b), we used the FAFB neuropil meshes corresponding to standard brain region definitions[72]. To identify brain regions containing presynaptic neurons (Fig. 4d-j), we calculated the cable length within each neuropil mesh (3D bounding box). The 2-4 brain regions containing the most cable were hand-traced in Adobe Illustrator and added to Fig. 4d-j.

Identifying a2 in the FlyEM dataset. We identified the FlyEM 'hemibrain' neuron 1140245595 as a2 based on its similarity to a2 in the FAFB dataset. Specifically, we considered (1) cell morphology, (2) the number of pre- and postsynaptic sites in the cell, and (3) the number of synaptic inputs to the cell from clearly identifiable presynaptic cell types (e.g., PFL3 neurons, LC9 neurons, and other cell types not shown). By all these criteria, the match was very good.

Optogenetic activation of a2

For the experiments in Fig. 8a-c and Supplementary Fig. 8, we used 2-3 day old females. Flies expressed FLP under the control of a heat-shock promoter, and they harbored *UAS-FRT.mCherry.FRT.ReachR.citrine* and *SS00730* transgenes. These flies were allowed to develop at room temperature (~21°C), as we found that this was sufficient to produce stochastic labeling. We took virgin flies from this culture and we fixed them into our standard platform. However, dissection was performed prior to making behavioral measurements, i.e. the head cuticle remained intact. After the flies acclimated to the spherical treadmill, orange light (617 nm, M617L3, Thorlabs) was delivered from above the head, so that the left and right sides of the head were illuminated symmetrically. The power density at the fly's head was 68 $\mu W/mm^2$. Light was switched on for 0.5 s every 11 s for a total of 150 trials. The experimenter remained blind to the fly's behavior throughout these trials. At the end of these trials, the dorsal cuticle was dissected away and ReaChR expression was scored. In a total of 73 experiments, we observed bilateral expression in 47 brains, left-only expression in 9 brains, right-only expression in 8 brains. and no expression in 8 brains. After ReaChR expression was scored, flies were divided into data analysis categories, and behavioral data was analyzed accordingly.

Optogenetic inactivation of a1 or a2

For the experiments in Fig. 8d-h, we used 2-3 day old females, comprising 7 control flies (empty-splitGal4), 11 flies where a1 expressed GtACR1 (*SS00731*), and 6 flies where a2 expressed GtACR1 (*SS00730*). Flies were kept on potato food infused with all-*trans* retinal (35 mM in ethanol; R2500, Sigma-Aldrich) for 24 hrs prior to behavioral testing. Flies were cold-anesthetized and placed in round arenas (38 mm in diameter) with transparent floors (clear acrylic, McMaster-Carr, 8536K134) and custom dome-shaped tops which were 3D-

printed with white resin to promote walking[73] and illuminated with diffuse overhead infrared light (850 nm ring LEDs, Alexnld). Flies were imaged from below using a camera (FLIR, BlackFly BFS-U3-13Y3M-C) equipped with a macro-zoom lens (Rainbow, S6X11). The lens was fitted with a 720 nm long pass filter (Hoya Filter, R72 Infrared) to block room light and optogenetic stimulation light. The video image was 1024 by 1280 pixels and was acquired at 60 Hz. Optogenetic stimulation was delivered using a green LED (Thorlabs, M530L4) positioned under the arena, and focused on the area of the arena using an aspheric condenser lens (Thorlabs, ACL25416U). Each experiment lasted 2 hrs, and during this time, the green LED was continuously cycled between on (2 min) and off (2 min). Videos were streamed to disk in 2-GB (27-s) chunks, while light on/off status was recorded using a custom Matlab program. In general, flies moved more with the light on, and this effect was quantitatively indistinguishable in the three genotypes. Therefore, we decided to focus on time windows where the fly was moving, in order to ask whether specific movement features are affected by DN silencing. For this reason, in the analyses below, we discarded data chunks where the fly's time-averaged translational velocity was <4.0 mm/s.

Data processing and analysis

Data alignment

Behavioral, stimulus, and imaging data were aligned using triggers acquired on the same NI-DAQ board.

Data analysis – spherical treadmill data preprocessing

Kinematic data used in computing linear filters, signal autocorrelations, LOWESS-fit scatter-plots, and event-triggered analysis were processed as follows. First, the zero-point of each kinematic signal was corrected for small artifactual offsets by finding the median of periods of inactivity, defined as regions with instantaneous difference of less than 0.025°/s. The offset value during these periods was largely consistent an entire experiment, so a global subtraction was used to remove this offset for each experiment.

We then lightly smoothed each kinematic variable by convolving with a 50-ms Gaussian kernel bounded from -3.5 σ to +3.5 σ, and re-normalized. In order to remove remaining high frequency noise while preserving large signal excursions, we then used Gaussian process smoothing. This smoothed the data by fitting the time series to a Gaussian random walk process and taking the maximum a posteriori probability (MAP) estimate for each time point, as found with the L-BFGS-B optimizer. The model was implemented with PyMC3[74]. Briefly, the model is as follows:

$$z_i \sim Normal\left(z_{i_{-1}} + \mu, (1-\alpha) * \sigma^2\right)$$
$$y_i \sim Normal(z_i, \alpha * \sigma^2)$$

Where each time point y_i was modeled as a draw from a normal distribution parameterized with mean $z_i + \mu$ and standard deviation $\alpha * \sigma^2$, where α acts as a factor to assign signal variance to a moving average or normally distributed noise. All variables except α were fit using the approximate inference software; μ was given a large initial prior standard deviation (100000, or 5-6 times the largest value present in the data) and it quickly converged to a stable value. We set α to 0.2 to assign 20% of signal variance to noise and the remaining 80% to the random walk. All time series were scrutinized to ensure proper baseline correction and smoothing.

Total speed was calculated by taking the absolute value of rotational velocity, sideways velocity, and translational velocity, and then summing these values:

total speed $= |r| + |s| + |t|$

where r, s, and t are all expressed in units of °/s (i.e. sideways and translational velocity were not yet converted into units of mm/s). This metric quantifies the overall level of fly movement, irrespective of the direction of movement.

Data analysis - electrophysiology data preprocessing

To compute mean changes in membrane voltage relative to baseline (mean Δvoltage) in Figs. 2b, 6f, and 7d (and Supplementary Figs. 6a and 7b), we first removed spikes by median-filtering the raw voltage trace. To compute firing rates in Figs. 1d-g, 2b, 3f-h, 6b,d,e, and 7b,c (and Supplementary Figs. 1a, 3a, 6a-c, 7d), we first detected spikes by using a relative prominence metric in the Matlab findpeaks function. We then counted spikes in 10-ms non-overlapping bins, and smoothed with an exponential filter using the smoothts function in Matlab with a 30-ms window size to generate a continuous waveform of firing rate versus time.

For Figs. 2d, 5, 6c, and 7e,f (and Supplementary Figs. 4 and 7c), firing rate was calculated as follows. First, data were conservatively band-pass zero-phase filtered using a first-order Butterworth filter with natural (3 dB) frequency of 100 Hz. Filtered time series were then normalized to a 500-ms rolling estimate of the median absolute deviation (MAD). MAD is defined as the median of absolute deviations from the median of the entire dataset. We used a corrected version of this estimate to maintain asymptotically Normal consistency by multiplying by 1.4826. This aids spike detection when firing rates are high. Spikes were then detected using the relative prominence metric in the find_peaks function in the SciPy Python library, where the prominence of a given spike was defined over a 10-s period. Prominence values were selected for each experiment and neuron. While requiring threshold tuning for some experiments, this method was robust in all a1 and a2 recordings. To estimate the firing rate, detected spikes were then binned at 1.25 ms and smoothed by convolving with a 2.5-ms Gaussian kernel as described above. All steps of firing rate calculation were scrutinized to ensure proper behavior by plotting periods known to be difficult or easy to estimate (i.e. small inter-spike-interval or high MAD).

To compute autocorrelations (Supplementary Fig. 4a,g) and linear filters (Figs. 5c-f, 6c, 7e,f, and Supplementary Fig. 4b-f,h-l), and for event-triggered analyses (Fig. 2d and Supplementary Fig. 7c), we processed electrophysiology data as follows. We first estimate an initial "offset" by taking the median of the first 30-60 s. We then median-filtered the entire time series using a kernel length of 35 ms. This window length was empirically selected to optimally preserve low-frequency voltage modulations while excluding most of the spike waveform. We then removed high frequency artifacts remaining after median filtering by convolving with a 5-ms Gaussian kernel (bounded from -3.5σ to +3.5σ and re-normalized). The resulting time series was then detrended by subtracting the average of linear fits to voltage data over every 30 s and 120 s, and then adding back the initial offset. All time series were scrutinized to ensure that median filtering and detrending were successful.

To compute neuron-behavior relationships, firing rates and membrane voltage values were downsampled to the same sampling rate as the spherical treadmill data. This was done by applying an upsampling by a factor of 4, applying a linear-phase finite impulse response filter, and then downsampling.

Data analysis - Signal autocorrelation analysis

Kinematic variable autocorrelation and neuron firing rate autocorrelation were calculated using the correlate function in the python library SciPy (Supplementary Fig. 4a,g) or Matlab's xcorr (Fig. 6b).

Data analysis - Linear filter analysis

Linear filters (Figs. 5c-f, 6c, 7e,f, and Supplementary Fig. 4b-f,h-l) were calculated using the sampling rate of the spherical treadmill data, meaning that electrophysiology data were downsampled as described in the preprocessing section. We calculated these linear filters by treating one signal as input and the other as output. We found the fast Fourier transform (FFT) of 1-sample overlapping 4-s windows of both input and output, and then computed

$$F(\Omega) = (input^*(\Omega) \times output(\Omega))/(input^*(\Omega) \times input(\Omega))$$

where $input^*$ represents the complex conjugate of $input$. The denominator of this equation is the input power spectrum, and the numerator is the cross-correlation between input and output in the frequency domain. We then applied the inverse of the fast Fourier transform to F to yield the linear filter relationship between input and output. For filter analyses, all behavioral variables were represented in units of °/s (i.e., sideways velocity and translational velocity were not converted from °/s to mm/s). This was done so that all filters had the same units (°/s in Fig. 5, or s/° in Supplementary Fig. 4), allowing direct comparison of different filter amplitudes.

Our input and output signals have little high-frequency content, and so division in the frequency domain introduces some noise into the linear filter. Moreover, each class of input-output relationship has its own characteristic frequency content. For this reason, we low-pass filtered the linear filters to remove this noise differently for each class. Behavior→Neuron filters were filtered with a 0th order Slepian window of 6 Hz bandwidth, whereas Neuron→Behavior filters were low pass filtered using a 0th order Slepian window of 15 Hz. These windows maximize energy in the central lobe and were empirically selected to avoid distortion of spectral content within the window.

To generate behavioral predictions, we convolved each cell's firing rate estimate with its Neuron→Behavior filters. To find the variance explained by each filter, we linearly regressed the predicted output against the actual output and took the R^2 value. Since each experiment differed in signal-to-noise, and low pass filtering was applied globally, the length of filter used in prediction was optimized within valid bounds for each neuron (100 ms to 4 s). In general, we found that a shorter filter was optimal for rotational velocity and sideways velocity, whereas a longer filter was optimal for translational velocity and total speed, consistent with the differing timescales of the autocorrelograms of these variables (Supplementary Fig. 4g). For generating a two-cell behavioral prediction from a2 dual recordings, we simply summed the predictions of both filters (Fig. 7e,f).

Data analysis - transitions between movement and immobility

To generate Fig. 2d, we defined total speed as $|r|+|s|+|t|$, as noted above, where r, s, and t are velocities expressed in units of °/s. We applied a threshold of 75°/s to the fly's total speed in each experiment in the increasing direction (to detect "starts") and also the decreasing direction (to detect "stops"). We then discarded starts where the fly was not consistently stopped before starting (i.e., in the window 750 ms before threshold crossing, 90% of data points were not less than or equal to ½ the threshold value), and we also discarded starts where the fly was not consistently moving after threshold crossing (i.e., in the window 750 ms after threshold crossing, 90% of the data points were not greater than the threshold value). Conversely, we also discarded stops where the fly was not moving consistently before stopping (i.e., in the window 750 ms before threshold crossing, 90% of the data points were not above the threshold value), and we also discarded stops where the fly was not consistently stopped after the threshold crossing (i.e. in the window after threshold crossing, 90% of the data points were not less than or equal to ½ the threshold value). Our conclusions based on this analysis were generally insensitive to the length of the window chosen. Finally, we aligned events by the time of threshold crossing, and we averaged data across events within each experiment before averaging across experiments.

Data analysis – transitions to backward walking

To generate Supplementary Fig. 7c, a threshold of -75°/s was applied to translational velocity in the decreasing direction. Events were accepted if they maintained the threshold value for 90% of a 75-ms window after threshold crossing, and if translational velocity was also >40°/s in 90% of the 200 ms prior to threshold crossing. We aligned events by the time of threshold crossing, and we averaged data across events within each experiment before averaging across experiments.

Data analysis – colormaps of behavioral data in 2-neuron space

To generate the colormaps in Figs. 6d,f and 7b,d (and Supplementary Figs. 3b,c, and 6a,b, and 7b), we shifted the neural data forward by 150 ms to account for the delay in behavior relative to neural data. We then divided both neural data and behavioral data into 50-ms nonoverlapping time windows. We computed the average firing rate or membrane voltage in each window; these values were then used to bin the behavioral data in 2-dimensional firing rate space or 2-dimensional membrane voltage space.

Data analysis - central complex stimulation

For the imaging data in Fig. 3b-h, imaging planes through the ellipsoid body (EB) were resliced to obtain coronal sections. Using custom Matlab code, we manually divided the EB into 8 equal wedge-shaped sectors. We then calculated ΔF/F for each EB sector, defining F as the average over time of the lower half of the raw fluorescence values for that sector.

We estimated the position of the bump of activity in E-PG neurons by computing a population vector average (PVA)[5]. Our experimental design required that we focus on trials where the bump was clearly visible and stable, jumped after the ATP puff, and then returned to its initial position; our goal was to study a2 neuron responses during this sequence of events. We therefore discarded trials where the bump amplitude faded during the trial – specifically, where PVA magnitude dropped below the 7th percentile (for that experiment) for more than 1 s during the trial. We then discarded trials where the bump was already moving during the 1 s prior to the ATP puff, meaning that the standard deviation of the bump's position during that period was >1.5 sectors. At this point, we computed the "initial position" of the bump in each trial as its mean position during the 1 s prior to the ATP puff. Next, we discarded trials where the bump did not jump in response to the ATP puff, i.e. where the bump's position did not move by at least 0.5 sectors. We also discarded trials where the bump did not return to dwell within 0.5 sectors of its initial position (i.e., its position before the bump jump) for at least 0.5 s. Our results were not especially sensitive to the precise values of any of these data inclusion criteria.

We defined the bump's return period as the time window beginning with the maximum excursion of the bump (from its initial position) and ending with the bump's return to a position within 0.5 sectors of its initial position. We found the time point during each trial where the bump's return speed was maximal. We then aligned trials by this time point before averaging data across trials and experiments. We confirmed that counterclockwise bump movements are generally associated with rightward behavioral turns, while clockwise bump movements are associated with leftward behavioral turns, as described previously[75].

Data analysis - optogenetic inactivation of a1 or a2

We removed 27-s video chunks where the fly moved less than one body length. We then cropped each chunk, with the field of view centered around the center of the fly, and we used these videos as inputs to the DeepLabCut[76] annotation software. In 1300 frames from 12 flies, we manually annotated 8 body parts in each frame: the tarsi of each leg, the posterior tip of the abdomen, and the center of the anterior edge of the head. Frames were chosen for manual annotation to maximize diversity of walking angles in the field of view. Training was performed on 95% of this 1300-frame dataset, and the remaining 5% was used to visually evaluate model performance by comparing the locations of manually labeled points and auto-labeled points. When the model mislabeled frames, it was generally because of an unusual walking angle or lighting condition, and so we added frames with these conditions to our training set and recomputed the detection model to improve performance in these situations. We also excluded stretches of data when the fly was grooming, jumping, or walking on the ceiling of the arena, because all these events reduced the model's performance. We labeled a leg "in stance" if the smoothed instantaneous velocity of the limb was <8 mm/s (averaged over 3 consecutive frames); otherwise the leg was labeled "in swing".

Sideways speed and rotational speed (Fig. 8e) Taking data from all three genotypes, we divided each video chunk into non-overlapping 500-ms windows. We then computed the vector between the head and the abdomen tip. We used this vector to compute the fly's translational velocity, sideways speed, and rotational speed, for each frame, averaged over all frames in the window. We discarded windows where the fly's average translational velocity was <2.0 mm/s. To determine whether there was a significant effect of a1 silencing on sideways speed or rotational speed, we performed a two-factor ANOVA with genotypes (a1/control) and light (on/off) as factors, and we examined the p-values associated with genotype×light interaction, after p-values were corrected for multiple comparisons (Bonferroni-Holm correction, m=2 tests). We used the same procedure to determine whether there was a significant effect of a2 silencing.

Leg movements associated with body rotation events (Supplementary Fig. 8 and Fig. 8f,g) We analyzed five metrics intended to capture the multi-leg kinematic features associated with body rotations. These metrics were based on previous descriptions of leg movements during body rotations[22,23]. Importantly, we determined the number of metrics we would test, and we fixed the exact definitions of those metrics, based on data from control genotypes alone. Our goal was to identify leg-kinematic features associated with body rotation in control flies, in order to subsequently determine if any of these features were altered when DNs were silenced. To analyze leg-kinematic features associated with body rotation, our first step was to detect body-rotation events by searching forward in time for moments where the fly's rotational speed exceeded a threshold of 20°/s and stayed above that threshold for at least 0.1 s. We then extracted a 500-ms window of data starting 100 ms prior to the threshold crossing. (We explored several window sizes, and chose 500 ms because it produced the strongest relationship between the multi-leg metrics and rotational movement, considering all five metrics taken together.). Next, for each leg, we detected every complete swing epoch and every complete stance epoch in the window. Then, in each window, we computed the following metrics (iF = inner front, iM = inner middle, iB = inner back, oF = outer front, oM = outer middle, oB = outer back):

1. *Stance direction* (Supplementary Fig. 8, row 1): The vector pointing backward along the body's long axis was taken as 0°. We measured each leg's movement direction (in body-centric coordinates) during each stance. When the fly is walking forward, leg stance directions are close to 0° (i.e., every leg is moving almost straight in the backward direction relative to the body). During left turns, the legs in stance tend to move rightward ($0° < \theta < 180°$), while conversely, during right turns, the legs in stance tend to move leftward ($0° > \theta > -180°$); see Supplementary Fig. $8b_1$. The stance direction metric was defined as the mean of the stance directions of the oF, iF, and iM legs (averaged over all epochs in the window).
2. *Swing direction* (Supplementary Fig. 8, row 2) The vector pointing forward along the body's long axis was taken as 0°. We measured each leg's movement direction (in body-centric coordinates) during each swing. When the fly is walking forward, leg swing directions are close to 0° (i.e., every leg is moving almost straight in the forward direction relative to the body). During left turns, the legs tend to swing leftward ($0° < \theta < -180°$), while conversely, during right turns, the legs tend to swing rightward ($0° > \theta > 180°$); see Supplementary Fig. $8b_2$. The swing direction metric was defined as the mean of the stance directions of the oF, iF, and iM legs (averaged over all epochs in the window).
3. *Swing distance* (Supplementary Fig. 8, row 3) We measured the distance each leg moved during its swing epochs. The swing distance metric was defined as the mean of the swing distances of the OF and OM legs (averaged across swing epochs), divided by the mean swing distances of the iM and iB legs (averaged across epochs in the window).
4. *Stance duration* (Supplementary Fig. 8, row 4 and Fig. 8f,g) We measured the time each leg spent in each of its stance epochs. The stance duration metric was defined as the stance duration of the iB leg (averaged over stance epochs), divided by the mean stance durations of the iF, oF, oM, and oB legs (averaged across epochs in the window).
5. *Swing duration* (Supplementary Fig. 8, row 5) We measured the time each leg spent in each of its swing epochs. The swing duration metric was defined as the mean swing duration of the iM and iB legs (averaged across epochs in the window).

To determine whether there was a significant effect of a1 silencing on any metric, we performed a two-factor ANOVA with genotypes (a1/control) and light (on/off) as factors, and we examined the p-values associated with genotype×light interaction, after p-values were corrected for multiple comparisons (Bonferroni-Holm correction, m=5 tests). We used the same procedure to determine whether there was a significant effect of a2 silencing.

Step frequency, step length, and translational velocity (Fig. 8h) We divided each video chunk into non-overlapping 500-ms windows. We discarded windows where the fly's time-averaged translational velocity was <2.0 mm/s. Step frequency was defined as the mean frequency of stance onset for all six legs, averaged across all complete stride epochs within that window, for all legs. Step length was defined as the mean stride distance of all six legs, averaged across all complete stride epochs within that window, for all legs. Translational velocity was defined as the velocity of the vector connecting the abdomen tip to the head, in the direction of that vector, for each frame, and then averaged over the window. To determine whether there was a significant effect of a1 silencing on any of these three variables (step frequency, step length, translational velocity), we performed a two-factor ANOVA with genotypes (a1/control) and light (on/off) as factors, and we examined the p-values associated with genotype×light interaction, after p-values were corrected for multiple comparisons (Bonferroni-Holm correction, m=3 tests). We used the same procedure to determine whether there was a significant effect of a2 silencing.

For the leg-centric metrics above, if any leg included in a given metric did not complete at least one of the relevant epochs during a particular time window, then that window was omitted. Moreover, for the ANOVAs described above, if a fly did not contribute at least 5 time windows to the dataset for that particular metric, then the fly was omitted. The number of flies that contributed data to each panel was as follows (control/a1/a2 genotypes): Fig. 8e (7/11/6); Fig. 8f,g (5/8/6); Fig. 8h – step frequency (6/8/6), step length (6/10/6), translational velocity (7/11/6). For Supplementary Fig. 8, the values are: row 1 (6/9/6); row 2 (6/9/6); row 3 (6/9/6); row 4 (5/8/6); row 5 (6/9/6).

Post hoc statistical tests: When any ANOVA yielded a significant genotype×light interaction, we followed up by performing a post hoc Tukey test to determine whether, for each genotype, there was a significant effect of light on/off. Finally, to confirm that it was reasonable to treat each time window as an independent datapoint, we performed a separate two-factor ANOVA with fly ID and light as factors, and we verified that variance due to fly ID is much smaller than total variance.

Data inclusion

In analysis of electrophysiology experiments, we excluded cells where the recording lasted <=15 minutes. Late in a recording, the membrane voltage sometimes became depolarized, which we interpret as a sign of poor recording quality; we therefore discarded any extended epoch where the membrane voltage was more depolarized than -33 mV.

In Figs. 1 and 2 (and Supplementary Fig. 2), flies were excluded that displayed highly asymmetric stimulus-evoked steering behavior. For example, we excluded a fly if on average, she displayed significant stimulation-evoked turns to the right but not to the left. These cases are likely due to asymmetric positioning of the fiber optic filaments near the antennae. This excluded 2/6 flies for fictive odor experiments and 3/7 flies for fictive warming experiments.

In Fig. 3, flies were excluded if there were <6 trials that passed the checks described above (see *Data analysis – central complex stimulation*). This excluded 4 of 8 recordings.

In single-cell recordings (Figs. 1, 2, 3, and 5; Supplementary Figs. 1a, 2, 3a, and 4), we excluded 1 a1 cell (out of

8 total) and 1 a2 cell (out of 11 total) where the recording quality fluctuated substantially over time.

DATA AND CODE AVAILABILITY

EM reconstructions will be archived at virtualflybrain.org. Code will be available at https://github.com/wilson-lab. Raw data are available upon reasonable request.

REFERENCES FOR ONLINE METHODS

53. Pfeiffer, B.*, et al.* Refinement of tools for targeted gene expression in *Drosophila*. *Genetics* **186**, 735-755 (2010).
54. Pfeiffer, B.D.*, et al.* Tools for neuroanatomy and neurogenetics in Drosophila. *Proc. Natl. Acad. Sci. U. S. A.* **105**, 9715-9720 (2008).
55. Jenett, A.*, et al.* A GAL4-driver line resource for *Drosophila* neurobiology. *Cell Rep.* **2**, 991-1001 (2012).
56. Lai, S.L. & Lee, T. Genetic mosaic with dual binary transcriptional systems in *Drosophila*. *Nat. Neurosci.* **9**, 703-709 (2006).
57. Frank, D.D., Jouandet, G.C., Kearney, P.J., Macpherson, L.J. & Gallio, M. Temperature representation in the *Drosophila* brain. *Nature* **519**, 358 (2015).
58. Chou, T.-b. & Perrimon, N. The autosomal FLP-DFS technique for generating germline mosaics in *Drosophila melanogaster*. *Genetics* **144**, 1673-1679 (1996).
59. Golic, K.G. & Lindquist, S. The FLP recombinase of yeast catalyzes site-specific recombination in the *Drosophila* genome. *Cell* **59**, 499-509 (1989).
60. Bloomington Drosophila Stock Center. Notes on X-linked insertions of heat shock-FLP constructs. ^https://bdsc.indiana.edu/stocks/recombinases/hsflp_notes.html, accessed April 1, 2020
61. Sutcliffe, B.*, et al.* Second-generation *Drosophila* chemical tags: Sensitivity, versatility, and speed. *Genetics* **205**, 1399-1408 (2017).
62. Inagaki, H.K.*, et al.* Optogenetic control of Drosophila using a red-shifted channelrhodopsin reveals experience-dependent influences on courtship. *Nature Methods* **11**, 325-332 (2014).
63. Hampel, S., Franconville, R., Simpson, J.H. & Seeds, A.M. A neural command circuit for grooming movement control. *eLife* **4**, e08758 (2015).
64. Chen, T.W.*, et al.* Ultrasensitive fluorescent proteins for imaging neuronal activity. *Nature* **499**, 295-300 (2013).
65. Klapoetke, N.C.*, et al.* Independent optical excitation of distinct neural populations. *Nat. Methods* **11**, 338-346 (2014).
66. Seelig, J.D.*, et al.* Two-photon calcium imaging from head-fixed Drosophila during optomotor walking behavior. *Nat. Methods* **7**, 535-540 (2010).
67. Zheng, Q.*, et al.* Rational design of fluorogenic and spontaneously blinking labels for super-resolution imaging. *ACS Cent. Sci.* **5**, 1602-1613 (2019).
68. Saalfeld, S., Cardona, A., Hartenstein, V. & Tomancak, P. CATMAID: collaborative annotation toolkit for massive amounts of image data. *Bioinformatics* **25**, 1984-1986 (2009).
69. Bates, A.S.*, et al.* The natverse: a versatile computational toolbox to combine and analyse neuroanatomical data. *bioRxiv 006353; doi: https://doi.org/10.1101/006353* (2020).
70. Cachero, S., Ostrovsky, A.D., Yu, J.Y., Dickson, B.J. & Jefferis, G.S. Sexual dimorphism in the fly brain. *Curr. Biol.* **20**, 1589-1601 (2010).
71. Longair, M.H., Baker, D.A. & Armstrong, J.D. Simple Neurite Tracer: Open Source software for reconstruction, visualization and analysis of neuronal processes. *Bioinformatics* (2011).
72. Ito, K.*, et al.* A systematic nomenclature for the insect brain. *Neuron* **81**, 755-765 (2014).
73. Simon, J.C. & Dickinson, M.H. A New Chamber for Studying the Behavior of Drosophila. *PLOS ONE* **5**, e8793 (2010).

74. Salvatier, J., Wiecki, T.V. & Fonnesbeck, C. Probabilistic programming in Python using PyMC3. *PeerJ Computer Science* **2**, e55 (2016).
75. Turner-Evans, D.*, et al.* Angular velocity integration in a fly heading circuit. *eLife* **6** (2017).
76. Mathis, A.*, et al.* DeepLabCut: markerless pose estimation of user-defined body parts with deep learning. *Nat. Neurosci.* **21**, 1281-1289 (2018).